Exploring sources of variation in thermoluminescence emissions and anomalous fading in alkali feldspars

RIEDESEL, S., BELL, Anthony <http://orcid.org/0000-0001-5038-5621>, DULLER, G.A.T., FINCH, A.A., JAIN, M., KING, G.E., PEARCE, N.J. and ROBERTS, H.M.

Exploring sources of variation in thermoluminescence emissions and anomalous fading in alkali feldspars

S. Riedesel[1], A.M.T. Bell[2], G.A.T. Duller[1], A.A. Finch[3], M. Jain[4], G.E. King[5], N.J. Pearce[1], H. M. Roberts[1]

[1]Department of Geography and Earth Sciences, Aberystwyth University, United Kingdom

[2]Materials and Engineering Research Institute, Faculty of Science, Technology and Arts, Sheffield Hallam University, United Kingdom

[3]School of Earth and Environmental Sciences, University of St. Andrews, St. Andrews, United Kingdom

[4]Department of Physics, Technical University of Denmark, DTU Risø Campus, Roskilde, Denmark

[5]Institute of Earth Surface Dynamics, University of Lausanne, Lausanne, Switzerland

Highlights

- TL emission spectra dependent on mineral phases, framework disorder and interfaces
- Single-phase feldspars show little anomalous fading
- Framework disorder increases intensity of blue TL emission and IRSL fading rate

Abstract

Alkali feldspar is routinely used in retrospective dosimetry using luminescence methods. However there is a signal loss over time, termed 'anomalous fading', which results in age underestimation if uncorrected. Although significant improvements have been made in recent years, luminescence dating of feldspars remains challenging. This paper investigates the relationships between chemistry, structural state and the scale of exsolution with thermoluminescence (TL) emission spectra and infrared stimulated luminescence (IRSL) fading rates.

We measure TL emission spectra, where possible linking the recombination site to physical features of the feldspar crystals. We show that fading rates are lowest in ordered end-member Na- and K-feldspars but significantly greater in disordered end-members, showing that Al-Si order influences fading. As well as having very low fading rates, ordered end-member samples have distinctive TL emission spectra, with the yellow-green emission dominant, while all other samples have a dominant blue emission. Perthite, i.e. exsolved members of the (Na,K)-feldspar solid solution, show greater fading than disordered end-members and fading is greatest in semi-coherent macroperthite. We propose that the state of Al-Si-order, and the occurrence of defects and dislocations at the perthite lamellar interfaces influence anomalous fading rates in feldspar.

Keywords

Alkali feldspar, thermoluminescence, emission spectra, fading rate, framework disorder

1 Introduction

Luminescence dating of feldspars is routinely conducted using the infrared stimulated luminescence (IRSL) signal and by measuring the emission in the blue (~410 nm) (e.g. Buylaert et al., 2012; Reimann et al., 2012; Smedley et al., 2016; Riedesel et al., 2018). However, feldspar IRSL dating has a major limitation, because it suffers from a signal loss at ambient temperatures, termed anomalous fading (Wintle, 1973; Visocekas, 1985), which results in age underestimation if uncorrected. A range of correction methods has been developed (e.g. Huntley and Lamothe, 2001; Kars et al., 2008), but these often result in large uncertainties on the final age. To circumvent the issues associated with having to quantify and try to correct for fading, research over the past decade has focussed on the isolation of an IRSL signal from feldspar that minimises anomalous fading. Lower fading rates have been obtained by increasing the stimulation temperature (Thomsen et al., 2008) and reduced further by using the signal arising from a second IR stimulation at elevated temperature (termed post-infrared infrared stimulated luminescence signal, post-IR IRSL, e.g. Thomsen et al., 2008; Thiel et al., 2011; Buylaert et

al., 2012), or by using a series of IR stimulations at increasing temperatures (termed multiple-elevated-temperature protocols, MET, e.g. Li and Li, 2011).

The cause of anomalous fading has been debated for more than 40 years (e.g. Wintle, 1977; Templer, 1986; Sanderson, 1988; Visocekas et al., 2014) and a loss of charge from electron traps over time, due to quantum mechanical tunnelling, is the most widely accepted explanation (e.g. Visocekas, 1985). The rate of anomalous fading has been linked to the density of available recombination centres (Huntley, 2006) and significant variations in the rate of fading have been observed in single-crystal feldspars (e.g. Spooner, 1992, 1994; Huntley and Lian, 2006) and in feldspar (single) grains extracted from sediments and bedrock (e.g. Neudorf et al., 2012; Trauerstein et al., 2012; Valla et al., 2016). Visocekas and Zink (1995) measured tunnelling afterglow in microcline and sanidine feldspars and inferred that increased anomalous fading of volcanic feldspars arises due to large concentrations of defects in the crystal caused by Al^{3+} and Si^{4+} disorder on the framework, and additionally due to the inclusion of Fe^{3+} on tetrahedral sites. Based on this observation, Visocekas and Zink (1995) suggested that ordered feldspars, such as microcline, could be dated, because their ordered structure would prevent fading. Indeed, Spooner (1994) observed a stable IRSL signal with the emission recorded between ~330 nm and ~630 nm (using 2 mm Schott BG39 filter) for one of his microcline feldspars and also for an Amelia albite specimen. In contrast, Huntley and Lian (2006) measured IRSL fading rates of the ~360 to ~620 nm emission (using BG39 and Kopp 4-97 filters) of up to 12 % in feldspars that they describe as microclines.

However, in most studies the samples are only characterised by their chemical composition, and although a description, which includes the structural state of the feldspar is often included (terminologies such as microcline or sanidine), no data are shown that proves this association. Thus it is difficult to compare fading rates measured with any other mineralogical property of the samples other than the chemical composition. Anomalous fading has often been observed and associated with the volcanic origin of the samples (e.g. Wintle, 1973; Visocekas and Zink, 1995, 1999; Guérin and

74 Visocekas, 2015). However, few fading feldspars used in luminescence dating are of volcanic origin
75 (e.g. Valla et al., 2016; King et al., 2016; Jenkins et al., 2018).

76 Due to exsolution in alkali feldspars during slow cooling in plutonic rocks, such as granite, feldspars
77 are often perthitic (e.g. Parsons et al., 2015). A relationship between interfaces in perthites and the
78 intensity of the UV emission (~290 nm) has been found (Garcia-Guinea et al., 1996). Baril (2004)
79 observed phase-dependent variations of violet and yellow luminescence emissions in perthites, and
80 Correcher et al. (2000) linked the blue luminescence in feldspars with alkali self-diffusion along
81 interfaces offset by hole centres. Spooner (1992) observed variable fading in his feldspars, which
82 contain Na and K. However, no clear relationship between exsolution features and anomalous fading
83 rates has yet been established. Additionally, earlier studies often analysed the IRSL signal of feldspars
84 with a wide emission range (e.g. Spooner, 1992, 1994; Visocekas and Zink, 1999; Huntley and Lian,
85 2006), likely including emissions arising from different defect types (cf. Krbetschek et al. (1997) for a
86 review on emission centres and associated crystal defects in feldspars). Developments within the last
87 decade have changed measurement protocols (e.g. Thomsen et al., 2008; Li and Li, 2011) and a wide
88 range of available optical filters enables the isolation of a narrow emission window, which allows a
89 specific emission to be selected. Thus, there is the need for a re-investigation of potential causes of
90 anomalous fading of the blue IRSL signal in chemically and structurally different feldspars.

91 This paper investigates the links between the blue luminescence emission, the anomalous fading rate
92 of the blue IRSL signal and multiple mineralogical characteristics in alkali feldspars. It explores
93 temperature- and wavelength-resolved variations in the blue luminescence intensity and variations in
94 anomalous fading rates of 12 single-crystal alkali feldspars, and three feldspar grain mixtures extracted
95 from bedrock and sediment. This suite of samples enables the investigation of potential relationships
96 between variations seen in the intensity and anomalous fading rate of the blue luminescence emission
97 and (i) the chemistry of the samples, (ii) the number of phases present in a single crystal specimen (i.e.
98 whether they are single phase or perthitic) and (iii) the degree of framework disorder of the samples.

2 Brief overview of the chemistry and structure of feldspars

The crystal lattice of feldspar is made up of $(Al,Si)O_4$ tetrahedra, each connected to four others by shared or "bridging" oxygen ions at their vertices, forming a continuous, interconnected framework. There are four tetrahedral positions within the framework (two of each of the so-called T_1 and T_2-sites), which are occupied by Si^{4+} or Al^{3+}. The framework has a net negative charge, which is offset by large cations (predominantly Na^+, K^+, Ca^{2+}) occupying cavities in the framework termed M-sites (Deer et al., 2013). The compositional variability of most feldspars is accommodated by three end members, each with a different M-site cation: $KAlSi_3O_8$ (K-feldspar), $NaAlSi_3O_8$ (Na-feldspar) and $CaAl_2Si_2O_8$ (Ca-feldspar). The solid solution between K- and Na-feldspars produces the alkali feldspar series; the solid solution between Na- and Ca-feldspar is termed plagioclase. There is very limited solid solution between K- and Ca-feldspar (<10 %). At high temperature (> 1000 °C), complete solid solution across the plagioclase and alkali feldspar series occurs (see Parsons 2010).

Here we consider the alkali feldspar solid solution series between K- and Na-feldspar. The structural state of alkali feldspar is an important indicator of the temperature of crystallisation and subsequent thermal history (Deer et al., 2013) and hence alkali feldspar is divided broadly into low- and high-temperature members. The structural state of low- and high-temperature alkali feldspars is dictated by the degree of ordering of Al and Si within the framework and, in the case of albite (Na-feldspar), coupled with displacive distortions to the framework. Ordered feldspar is equilibrated at low (e.g. <300°C) temperatures. Generally, increased ordering of Al and Si within the framework takes place during slow cooling, e.g. in plutonic rocks. During rapid cooling a disordered distribution of Al and Si at high temperatures is quenched (e.g. sanidine, the monoclinic K-feldspar in volcanic rocks) (Deer et al., 2013).

The progressive ordering in alkali feldspars can be understood in terms of the distribution of Al^{3+} on the framework. In the high-temperature K-feldspar (monoclinic high sanidine), Al^{3+} has an equal (25 %)

chance of occupying any of the four tetrahedral sites ($T_1(0)$, $T_1(m)$, $T_2(0)$ and $T_2(m)$) within the more open alkali feldspar framework. During slow cooling, as the framework contracts, Al^{3+} diffuses to occupy preferentially one of the two T_1-sites (giving the monoclinic low sanidine). With continued slow-cooling, Al^{3+} preferentially diffuses into one of the T_1-sites ($T_1(0)$, see Parsons 2010), causing a change in symmetry from monoclinic (sanidine, with the greatest disorder) to triclinic, the ordered K-feldspar maximum microcline (Deer et al., 2013). Associated with this drop in symmetry, microcline adopts repeated twinning in two different orientations visible in a polarising microscope, termed 'tartan' or 'tweed' twinning (Deer et al., 2013).

Although alkali feldspar is a continuous solid solution at high temperature, the small ionic radius of Na^+ (0.118 nm) triggers a displacive collapse of the framework around Na^+ as the structure attempts to maintain bonding to the smaller Na^+ ion. The feldspar framework cannot collapse around the larger K^+ ion (0.151 nm), hence the alkali feldspar solid solution becomes unstable on cooling and unmixing ('exsolution') of the K- and Na-rich phases in alkali feldspar occurs. Such alkali feldspars are single crystals comprising intergrowths of separate K- and Na-rich feldspars, termed 'perthite'; perthites are further divided into crypto-, micro- and macroperthite, dependent on the scale of the intergrowths (from sub-optical, nanometre scale cryptoperthite, microperthite with lamellae visible under a petrographic microscope, and macroperthite whose lamellae are visible to the naked eye). The cooling rate and fluid interaction after crystallisation of the magma influence the size of the perthite lamellae, with cryptoperthite forming earlier in cooling (Brown and Parsons, 1984a) and coarsening over time. Fluid interaction is involved in the coarsening process of micro- and macro-perthite (e.g. Parsons, 1978). Near-pure Na and K feldspars may occur in a variety of environments including deep, high pressure (>0.5 GPa) or high-water content crystallisation of granites/pegmatites (including samples used here e.g. from Minas Gerais, Brazil, CLBR, Table 1, Cassedanne and Roditi, 1996) or wet (low-intermediate grade) metamorphic settings (e.g. albite Al-I, Table 1, Govindaraju, 1995). In these cases, the alkali-feldspar phase relationships during various combinations of slow-cooling, water content and magma/protolith composition can produce almost pure end-member ordered alkali feldspars (see

Deer et al., 2013, Parsons, 1978; Parsons et al., 2005). The homogeneity of samples from some of these "exotic" environments (e.g. pegmatites) mean that such pure end-member samples are often used as reference materials or samples for experimentation.

3 Material and methods

3.1 Samples

The samples used in this study can be split into two groups, single crystal feldspar specimens and examples of feldspars routinely used for sediment dating and luminescence thermochronometry. The chemical composition of the samples and the mineral phases present were determined by X-ray fluorescence (XRF) and X-ray diffraction (XRD), respectively. Additionally, the samples were examined optically for their colour and the coarseness of any perthite lamella that may be present. We combined our visual inspection, following the definition of perthite microstructures by Deer et al. (2013, p. 253), and the results of the semi-quantitative phase analyses using XRD to separate the perthitic samples into two groups: Both groups have in common that they were determined to be two-phase using XRD. One group of perthites has K- and Na-feldspar lamellae on the optical scale, so that we were able to identify them by eye or using a hand lens. We refer to these feldspar samples as macroperthite. The second group consists of perthite where XRD results defined them as two-phase, but where we were unable to see the lamellae with the naked eye or even through an optical microscope. We refer to these feldspars as cryptoperthite.

The chemical composition of the samples was determined by XRF. For XRF measurements 2 g of cellulose binder was placed into an Al sample boat. Powdered sample (0.1 g) was then mixed with cellulose binder (0.1 g) and this mixture was spread on top of the cellulose binder in the Al sample boat. Each boat was then pressed at 20 t to pellets for XRF measurements using a PANalytical MagiX

PRO XRF spectrometer equipped with a Rh anode X-ray source. The spectra were collected over ten different energy ranges and then analysed to obtain semi-quantitative results. For the analyses, it was assumed that all elements, except for Cl, were present as oxides. The chemical composition of all samples is summarised in Table S1. Individual sample compositions were calculated to give the molecular formula of the feldspar based on eight oxygen, following stoichiometry. The results are shown in Figure 1A and given in Table 1.

Semi-quantitative phase analysis results of the samples were obtained using XRD. The measurements were carried out using a PANalytical X'Pert MPD powder diffractometer operating with Cu Kα X-rays and a PIXCEL-1D area detector. For these measurements 0.1 g of powdered sample was mounted on a low-background silicon XRD sample holder using acetone. Data were collected over the range of 5-100 degrees 2θ, each scan took just over 1 hour.

Because of the limited availability of sample material for samples R1-11A and CLBR, and since very detailed characterisation is already published, detailed XRF and XRD measurements were not performed. The chemistry and mineralogy of R1-11A was investigated in detail by Harrison et al. (1990) and the results from their study are used here and are presented in Table 1. The chemical composition determined by Harrison et al. (1990) is based on electron probe microanalyses. Rendell and Clarke (1997) and Garcia-Guinea et al. (1999) performed luminescence experiments and mineralogical investigations of CLBR and determined its structural state as low albite. Additionally, Riedesel et al. (2019) assessed its chemical composition using an XRF detection head attached to a Risø TL/OSL reader (Kook et al., 2012; and see the supplementary material of Stevens et al., 2018). For this measurement a shard of the sample (~1 mm diameter) was placed on a Mo cup (without silicone spray) and the chemical composition was measured three times. The result of this measurement procedure is given, alongside the chemistry of the other samples, in Table 1.

Details regarding the origin of the samples, their chemical composition and mineralogical properties as determined using the analyses described above are given in Table 1 for the single crystal specimens,

and in Table 2 for bedrock and sediment extracts. Single-phase feldspars included in the sample suite are single-phase microcline (FSM-13), and single-phase albite (CLBR and Al-I). Note that Al-I includes 5 % quartz, based on semi-quantitative XRD measurements. Photoluminescence and excitation spectra of CLBR were presented by Riedesel et al. (2019, referred to as Cleavelandite).

FSM-5 and FSM-11 are macroperthite, with the perthite lamellae visible with the naked eye. Based on semi-quantitative phase analyses using XRD the phases present in these two samples are albite and microcline. Cryptoperthite are R1-11, FSM-3, FSM-7, FSM-8 FSM-14 and FSM-15. The perthite phases are microcline and albite in the case of R1-11A, FSM-3, FSM-7, FSM-8, FSM-14 and FSM-15, and orthoclase and albite for FSM-6, as determined using XRD. Photoluminescence, excitation spectra and cathodoluminescence of R1-11A were presented by Riedesel et al. (2019) and Finch and Klein (1999).

WHB-7, the density separated feldspar extract from unconsolidated sediment, consists of microcline and albite, but XRD also showed the presence of muscovite and quartz. HAM-5, another feldspar extract from sediment, consists of orthoclase, albite, quartz and illite, based on semi-quantitative XRD results. The thermochronometry sample MBT-I-2430 consists of feldspar only, in this case microcline and albite. Excitation spectra of HAM-5 and MBT-I-2430 were presented by Riedesel et al. (2019).

Whilst all these samples allow us to investigate the influence of differences in the chemical composition and the mineral phases, laboratory heating experiments on FSM-6 and FSM-13 were conducted to enable the investigation of potential effects of framework disorder on the luminescence emissions and fading rates.

To explore the effect of Si and Al disorder on luminescence properties, 0.5 g of powdered sample material of samples FSM-6 and FSM-13 (referred to as FSM-6LH and FSM-13LH after heating) were placed in acid cleaned Pt crucibles and heated to 105 °C overnight to remove any potential liquid present in the sample material. The Pt crucibles with the sample material were then placed in a preheated furnace at 1050 °C and covered with fitted Pt lids. The samples remained in the furnace at 1050 °C for 5 days (FSM-6LH) and 10 days (FSM-13LH) to allow disordering of Si and Al on the

framework. To keep the disordered structure, the samples were rapidly cooled by placing the Pt crucibles in cooled sample holders. Comparison of X-ray diffraction patterns of the unheated and heated material of samples FSM-13/FSM-13LH and FSM-6/FSM-6LH reveals differences linked to states of Al-Si order (Fig. 1B, C). The (131) diffraction peak indicates the triclinicity of the material (a narrow single peak if the sample is triclinic, two peaks if the sample is monoclinic, e.g. Garcia-Guinea et al., 1999). Firstly, Figure 1B and C indicate different degrees of disorder of the two starting materials of FSM-13 and FSM-6 in their X-ray diffraction pattern. Whilst the XRD pattern of FSM-13 shows two fully defined diffraction peaks (131 and $1\bar{3}1$) between 29° and 32° 2θ, FSM-6 shows only a single peak (131) at 29.8° 2θ with a minor peak ($1\bar{3}1$) around 30° 2θ. This supports results from semi-quantitative phase analyses, based on which FSM-13 was defined as microcline and FSM-6 as two-phase consisting of albite and orthoclase (Table 1). Samples described as orthoclase are microcline with incomplete order of Al^{3+} on T_1-sites (Deer et al., 2013, p. 256-257) Secondly, as a result of the heating experiment, the two individual peaks in the diffractogram of FSM-13 (Fig. 1B) move closer together (see red line) and the minor diffraction peak in the diffraction pattern of FSM-6 (Fig. 1C) disappears and only a single diffraction peak around 30° 2θ is visible after heating (FSM-6LH, Fig. 1C, red line). This shows that the heating experiment is successful in disordering both samples, but that the heated material of FSM-6LH is relatively more disordered compared to FSM-13LH.

In addition to changes of tetrahedral site occupancy by Al^{3+}, prolonged heating is expected to influence the distribution of K^+ and Na^+ ions within the perthitic sample FSM-6. Whilst semi-quantitative phase analyses of the unheated sample FSM-6 characterised it as two-phase, with albite and orthoclase as the phases present, the heated sample FSM-6LH is defined as sanidine by XRD, where Na^+ and K^+ ions are distributed randomly throughout the crystal and not separated in perthite lamellae of K- and Na-feldspar. This becomes apparent when comparing the position of the ($\bar{2}01$) diffraction peak (Deer et al., 2013, p. 260). In the X-ray diffraction pattern of perthitic sample FSM-6 are two ($\bar{2}01$) peaks, one for each phase (at 20.98° 2θ for the microcline phase, at 22.01° 2θ for the albite phase). In contrast, there is only a single ($\bar{2}01$) diffraction peak in FSM-6LH at 21.25° 2θ (Fig. 1D).

We also attempted Rietveld refinement, to refine the crystal structure and to quantify the tetrahedral site occupancy by Al^{3+} and Si^{4+} ions. However, due to a strong preferred orientation of the sample material a quantification of the tetrahedral site occupancy was not possible. When using XRD in this manner, we recognise that XRD is a measure of long-range tetrahedral site order (i.e. the development of large, e.g. 100s nm, ordered domains) and relatively insensitive to local short-range order which is better explored by local probes such as Nuclear Magnetic Resonance (NMR, Xiao et al. 1995).

3.2 TL emission spectra

Thermoluminescence (TL) emission spectra were measured using an Andor spectrometer (Prasad, 2017) attached to a Risø DA20 TL/OSL reader equipped with a $^{90}Sr/^{90}Y$ beta source delivering ~0.1 Gy/s at the sample position and a DASH (Lapp et al., 2015). The single-photon EMCCD-based spectrograph, used to record the spectra, is attached to the Risø reader via a fibre optic bundle cable. The thermoelectrically cooled EMCCD camera (Andor iXon Ultra 888) has a 1024 x 1024 sensor format and a pixel size of 13 µm. The spectral resolution of the system is 13 nm for all spectra recorded. The TL signal was recorded without any optical filters, to allow the emission spectrum to be recorded in a wide range of wavelengths (~280 to ~720 nm). The grating of the spectrograph was set to 150 lines/mm and 500 nm blaze. The resulting spectra consist of 1024 bins, ranging from 280.68 nm to 718.94 nm, with a bin width of 0.43 nm. The electron-multiplying gain (EM) varied for individual measurements, dependent on the sample brightness, except for the unheated and heated material of FSM-13/FSM-13LH and FSM-6/FSM-6LH, where the EM gain was kept the same, to allow absolute signal intensity comparisons.

For TL spectra measurements, samples were placed on stainless steel cups and were beta irradiated using different doses (ranging from 60 to 1,000 Gy), to yield optimal signal output for the samples analysed. To be able to compare absolute intensities for the unheated and heated material of FSM-13 and FSM-13LH as well as FSM-6 and FSM-6LH the same sample mass (10 mg) and irradiation dose

were used (400 Gy for FSM-13 and FSM-13LH; 200 Gy for FSM-6 and FSM-6LH). A 1000 s pause was inserted after irradiation to allow potential phosphorescence to decay prior to the TL measurement up to 380 °C (heating rate 1 °C/s). A second TL measurement was performed, immediately after the first and used for background subtraction. Repeat measurements were performed and the impact of changing the size of the given dose was tested, to check for reproducibility. All spectra were corrected for the response of the instrument.

3.3 IRSL fading measurements

Infrared stimulated luminescence (IRSL) fading measurements were performed using Risø DA20 TL/OSL readers equipped with $^{90}Sr/^{90}Y$ beta sources delivering ~0.03 Gy/s and ~0.1 Gy/s at the sample position. Sample material was placed on stainless steel cups. Typically, three aliquots per sample were measured.

Fading was measured for a signal in response to ~90 Gy using a post-$IR_{50}IRSL_{225}$ protocol (Table 3) with a preheat at 250 °C for 60 s. The test dose signal was measured after a beta dose of ~30 Gy. The $IRSL_{50}$ and post-IR $IRSL_{225}$ signals were recorded through a combination of a Schott BG39 and a Corning 7-59 filter (transmission greater than 10 % from 340 nm to 470 nm) using a UV-sensitive photo-multiplier tube (PMT). To ensure stable heating for the IRSL signal measurements, the sample was held at the measurement temperature for 30 s, prior to switching on the IR LEDs. Due to the high signal intensities of FSM-13LH, a ND 1.0 filter was added to the blue filter combination. Delays between different fading measurements ranged from prompt measurements with delays of ~500 to ~800 s between the end of irradiation and luminescence measurement, depending on the instrument, to at least 1,000,000 s. For both signals investigated, the first 10 s were integrated as a signal, and background corrected by subtracting the signal integrated over the last 20 s of each decay curve. Fading rates, expressed as g-values, were calculated using the Analyst software (Duller, 2015) and all g-values presented are normalised to two days (Huntley and Lamothe, 2001).

4 Results

4.1 TL emission spectra

TL emission spectra of all samples investigated are recorded in the wavelength range from 280 to 720 nm and will thus give insights into recombination centres which emit in this part of the electromagnetic spectrum. The main emissions observed are centred at ~300 nm, ~400 nm, ~550 nm and >700 nm (e.g. Krbetschek 1997). However, the intensity of these emissions and the temperature at which the emissions occur varies between samples. The emission spectra from the samples can be divided into four groups: those from single-phase feldspars, perthite with lamellae visible with the naked eye (macroperthite), perthite with lamellae on the sub-optical scale (cryptoperthite) and feldspar extracted from sediments and bedrock, which may contain grains of numerous, (possibly different) feldspar group minerals.

The emission spectra recorded for the single-phase feldspars (FSM-13, Al-I and CLBR, Fig. 2), show their brightest emission around 550 nm. Additionally, all three samples show an emission around ~300 nm. The two albite specimens (CLBR and Al-I) also show an emission in the blue (~400 nm) and sample Al-I a tail of a red emission around ~720 nm. The emissions at ~300 and ~550 nm of FSM-13 are most intense at ~100 °C (Fig. 2). The temperatures at which the emissions of Al-I and CLBR show their maximum intensity differ slightly for each emission (Fig. 2). For Al-I, the peak of the red emission occurs at the lowest temperature (~100 °C). This is followed by the relatively weak blue emission around ~150 °C and the UV (~300 nm) and yellow-green emission (~550 nm) peak around ~170 °C (Fig. 2). Whilst FSM-13 and Al-I show one TL peak at any given emitting wavelength, CLBR displays a number of TL peaks. The strongest emission for CLBR, the yellow-green, shows a low temperature peak around ~95 °C, a second peak at ~170 °C and a shoulder around ~250 °C. Similar behaviour is also visible for the weaker blue emission around ~400 nm. The UV emission (~300 nm) also emits around ~95 °C and around ~170 °C (Fig. 2).

Perthite in this study are divided into macroperthite and cryptoperthite. Figure 3 shows the emission spectra for all cryptoperthite used in this study. The emission spectra of these samples commonly share a broad emission ranging from ~350 to ~600 nm. Mostly this emission occurs around ~100 °C (Fig. 3), but R1-11A (Fig. 3B) and FSM-7 (Fig. 3F) also show an emission tail towards higher temperatures, resulting in a minor peak around ~350 °C for the emission centred around ~400 nm (Fig. 3). Additionally, all cryptoperthite show the short wavelength tail of a red emission (~700 nm). This emission is strongest for sample FSM-15 (Fig. 3C), a pinkish cryptoperthite, which contains 0.2 wt% Fe (Table S1).

The emission spectra of the macroperthite samples FSM-5 and FSM-11 (Fig. 4A and B) are similar to those of the cryptoperthite (Fig. 3), as the emissions of these two samples also occur at low temperature (~100 °C). However, the macroperthite show a stronger red emission, compared to the broad blue to yellow emission, which was observed as being dominant in the majority of the cryptoperthite with the exception of FSM-15 (compare Fig. 3 and 4). All emissions for these two samples exhibit a peak at the same temperature (Fig. 4). Sample FSM-11 contains 0.5 wt% Fe, which is consistent with this dominant red emission, though the XRF data for FSM-5 registers no Fe above the detection limit.

Further investigation focuses on the effect of prolonged heating to 1050 °C in a furnace and subsequent rapid cooling on TL emission spectra of single-phase feldspars using samples FSM-6LH and FSM-13LH. Figure 6 shows the TL emission spectra for FSM-13 and FSM-13LH, the latter was artificially disordered through heating and rapid cooling as described in section 2.1. The TL spectrum of FSM-13 shows a dominant emission around ~550 nm and a dimmer one around ~300 nm (Fig. 5). A weak blue emission (~400 nm) is also present. The maximum intensity of the TL spectrum of FSM-13 of just over 3000 cts/°C/0.4 nm is recorded around ~560 nm and at ~100 °C (Figs. 5A and C). The emission spectrum of FSM-13LH differs from the spectrum of FSM-13. FSM-13LH shows its main emission in the blue region of the spectrum, with a peak emission of over 40,000 cts/°C/0.4 nm around ~150 °C (Fig

348 5B). Additionally, the signal now spreads towards higher temperatures, with the blue emission
349 showing a secondary peak around 350 °C (Fig. 5D). A similar shift towards an emission at higher
350 temperature is observed when comparing the TL emission spectra of FSM-6 and FSM-6LH (Fig. 6).
351 Whilst FSM-6 already emitted in the blue region prior to disordering, the spectrum of disordered FSM-
352 6LH shows intensities in the blue emission twice as large as recorded for its unheated counterpart and
353 a narrowing of the emission peak is also observed (Fig. 6A and B). On the basis of the findings for
354 samples FSM-13LH and FSM-6LH, we observe that disordering results in i) an increase in the intensity
355 of the blue luminescence and ii) a shift of the TL emission peak temperature towards higher
356 temperatures.

357 To relate features observed from TL emission spectroscopy of single crystals to material generally used
358 in luminescence dating or thermochronometry, TL spectra were recorded from feldspar extracts from
359 sediments (WHB-7, Fig. 7A and HAM-5, Fig. 7B) and bedrock (MBT-I-2430, Fig. 7C). The emission
360 spectra of these sand-sized feldspar grain mixtures show similar characteristics to the perthitic
361 samples: TL maxima mainly around ~100 °C, a broad emission ranging from ~350 to ~600 nm, and the
362 tail of the red emission (Fig. 7).

363 **4.2 Fading rates**

364 Fading measurements were performed on all samples using a post-$IR_{50}IRSL_{225}$ protocol (Table 3). This
365 protocol is chosen as it enables the measurement of two IRSL signals, one at low temperature (50 °C),
366 and a second IRSL signal measured at elevated temperature (225 °C). The data from all $IRSL_{50}$ fading
367 measurements, shown as L_x/T_x ratios after different delays, are presented in Figures S1 to S4 in the
368 supplementary material. In agreement with results shown by Thomsen et al. (2008), we observe
369 consistently lower fading rates for the post-IR $IRSL_{225}$ signal compared to the fading rates of the $IRSL_{50}$
370 signal of our samples (Table 4). We also observe a proportional relationship between the fading rates
371 obtained for the two IRSL signals (Fig. 8A). Şahiner et al. (2017) have shown that the first IRSL
372 measurement step in a post-IR IRSL or post-IR-MET procedure results in the recombination of

electrons with the most proximal recombination centres, implying that fading of this first IRSL measurement can give information on the proximal recombination centres. All g-values (%/decade) presented in the following discussion are those obtained for the $IRSL_{50}$ signal. The average g-value (± 1 standard deviation) for each sample is shown as a function of their K-feldspar content in Figure 8B.

Single-phase albite (CLBR and Al-I) show the lowest fading amongst this suite of samples for the $IRSL_{50}$ signal, resulting in g-values of 0.36 ± 0.60 and 0.58 ± 0.30 %/decade respectively. The other single-phase sample (microcline FSM-13) was unique in giving very variable g-values, and hence nine sub-samples were measured. Five aliquots yielded g-values of less than 1%/decade (n = 5, average value is -0.23 ± 0.76 %/decade), one aliquot gave 1.14 ± 0.72 %/decade, and the three others showed fading rates between 2.00 and 3.12 %/decade. Considering the data together by calculating the average and standard deviation results in a very low g-value but with a high uncertainty (0.93 ± 1.52 %/decade, n = 9). The reason for the variability is not known, but we hypothesise that it is due to small-scale variations of structural state within the sample. Solid solutions of microcline are rarely found in nature and, although this sample was determined as single phase microcline, we cannot exclude perthitic patches or local Al disorder within the sample, which cannot be detected by XRD, but which may influence the fading rates.

The second group of samples are perthites. The macroperthites (FSM-5 and FSM-11) exhibit the highest fading rates (8.99 ± 1.82 %/decade, FSM-5, n = 3; and 12.42 ± 1.71 %/decade, FSM-11, n = 3). Cryptoperthite show fading rates ranging from 1.80 ± 0.32 %/decade (FSM-8, n = 3) to 6.72 ± 2.51 %/decade (R1-11A, n = 3), but all the values are below those recorded for macroperthite.

The effect of framework Al disorder on the fading rate was explored using the artificially disordered samples FSM-6LH and FSM-13LH. Heated sample FSM-6LH showed an increase in fading (4.99 ± 0.20 %/decade, n = 3), compared to the unheated material (FSM-6, 2.75 ± 1.47 %/decade, n = 3); similarly, an increase in fading rate is observed for disordered FSM-13LH (3.24 ± 0.16 %/decade (n = 3), compared to 0.93 ± 1.52 %/decade (n = 9) for FSM-13).

Fading measurements were also performed on feldspars extracted from sediment and bedrock samples, to allow a comparison to material routinely used in luminescence dating studies. Here the fading rates measured are within the range of those determined for cryptoperthite. $IRSL_{50}$ fading rates for sediment samples WHB-7 and HAM-5 are 3.07 ± 0.74 and 1.86 ± 0.46 %/decade, respectively, while the fading rate for the bedrock sample MBT-I-2430 is 3.28 ± 0.14 %/decade.

5 Discussion

5.1 Thermoluminescence emissions in chemically and structurally different alkali feldspars

The TL emission spectra reveal significant differences in emission centres for single-phase feldspars in comparison to the perthites, particularly regarding the presence and intensity of the blue emission. Single-phase microcline (FSM-13) and albite (CLBR and Al-I) show little blue emission, compared to a relatively intense yellow-green emission, and additionally, an emission in the UV is present in the TL spectra of these samples (Fig. 2). In contrast, in perthitic feldspars (Fig. 3 and 4) the blue emission is dominant, only surpassed in intensity by the red emission in macroperthite (FSM-5 and FSM-11, Fig. 4) and cryptoperthite FSM-15 (0.2 wt% Fe, Fig. 3C). Disordering of samples FSM-13 (single-phase microcline) and FSM-6 (perthite: albite and orthoclase) results in an increase in the blue emission intensity recorded for FSM-13LH and FSM-6LH (Fig. 5 and 6). These results are consistent with the blue emission in alkali feldspars being associated with (dis)-ordering of the framework (Finch and Klein, 1999) and with the observed sensitisation of the blue emission due to alkali ion leakage caused by prolonged heating (Garcia-Guinea et al., 1999).

The defect giving rise to the blue emission in feldspars has been under investigation since the early 1980's and it has been suggested that it arises either due to a hole centre located on an Al-bridging oxygen ion (Al^{3+}-O^{1-}-Al^{3+}, e.g. Speit and Lehmann, 1982a; Finch and Klein, 1999) or (for plagioclase) due to Eu^{2+} substituting for Ca^{2+} on M-sites (Götze et al., 1999). A solution involving the silicate framework is the most likely and in alkali feldspar, where Ca^{2+} concentrations are minor (e.g. Table 1), a hole

422 centre on an Al-bridging O is the most likely explanation and is consistent with the results of the
423 present study. The Al-O-Al bridge will only occur where there is a degree of Al-Si framework disorder
424 and it is hypothesised that it is stabilised at low temperatures by the addition of an electron hole (Speit
425 and Lehmann, 1976; Speit and Lehmann, 1982b, Finch and Klein 1999). This is consistent with the
426 spectra recorded for single-phase albite and microcline (CLBR, Al-I and FSM-13), which show very little
427 blue TL emission (Fig. 2). Artificially induced disorder in the microcline sample FSM-13 enhances the
428 blue emission in FSM-13LH, again supporting a model in which Al disorder is implicated in the blue
429 emission intensity. However, the perthitic feldspars are two-phase mixtures of albite and microcline,
430 both of which are partially ordered (Table 1). All perthitic feldspars investigated here emit in the blue
431 (Fig. 3).

432 Garcia-Guinea et al. (1999) linked the UV emission to twin interfaces in the feldspar end-members.
433 Albite and microcline both have multiple twinning, the result of the inversion from monoclinic to
434 triclinic symmetry during cooling. Supporting this, Polymeris et al. (2013) observed more intense UV
435 TL emission in ordered microcline, compared to disordered sanidine. Microcline shows repeated
436 twinning, whilst sanidine does not (cf. Deer et al., 2013, p. 253). In perthite, the possible interfaces
437 include not only the twins within each component phase, but also the interfaces between the K- and
438 Na-feldspar end-members. According to heating experiments (Garcia-Guinea et al. 1999),
439 luminescence attributed to twins contributes to the UV and part of the broad blue emission in perthite
440 (cf. TL spectra in Fig. 3). This is supported by Correcher et al. (2000), who linked the blue luminescence
441 in feldspars with alkali self-diffusion along interfaces offset by hole centres.

442 Perthitic feldspar FSM-6 shows an emission in the blue region. Prolonged heating of the sample
443 material disordered both the Na- and K-feldspar end members, thereby reducing strain at the
444 interfaces and (if accompanied by Na and K diffusion) creating single-phase alkali feldspar with a
445 sanidine structure (FSM-6LH, Table 1, Fig. 1D). Associated with this heating, we observe that the blue
446 TL shifts towards higher temperatures, the emission band narrows and the signal intensity doubles

447 from 10,000 to 20,000 cts/°C/0.4 nm (Fig. 6). This increase supports the suggestion that disorder of Si
448 and Al is implicated in the intensity of the emission.

449 Whilst the blue emission is absent or weak in single-phase albite and microcline, the yellow-green
450 emission (~550 nm) is a key feature of their spectra (Fig. 2). Interestingly, this emission has been
451 associated with Mn^{2+} substituting for Ca^{2+} on M-sites in plagioclase (e.g. Geake et al., 1971; Telfer and
452 Walker, 1978), but it is also present in microcline sample FSM-13. This microcline sample has no
453 detectable CaO content (Table S1) and hence it is unlikely that the emission around ~550 nm of this
454 sample is related to Mn^{2+}. Based on lifetime measurements of the green-yellow emission in a Na-
455 feldspar sample, Prasad et al. (2016) argued that Mn^{2+} substituting for Ca^{2+} on M-sites cannot explain
456 this emission; its recombination lifetime was too short for spin-forbidden Mn^{2+} transitions. Further
457 work is needed to identify the physical nature of this recombination centre but we concur with the
458 findings of Prasad et al. (2016) that it is inconsistent with Mn^{2+}.

459 **5.2 Fading rates of chemically and structurally different alkali feldspars**

460 Fading rates measured for the $IRSL_{50}$ signal (Table 4, Fig. 8B) of chemically and structurally different
461 alkali feldspars range from 0.36 ± 0.6 %/decade (CLBR, n = 3) to 12.42 ± 1.71 %/decade (FSM-11, n =
462 3). Single-phase feldspars show the least fading, whilst macroperthites (FSM-5 and FSM-11)
463 demonstrate the highest fading rates. Cryptoperthite show a similar fading behaviour to samples
464 extracted from bedrock (MBT-I-2430) and sediment (WHB-7, HAM-5), and the fading rates observed
465 for these, range in between those measured for macroperthite and single-phase feldspars (Table 4,
466 Fig. 8B).

467 The low fading rates of the blue emission of the $IRSL_{50}$ signal for single-phase albite and microcline
468 samples coincide with the relatively low blue luminescence signal intensities of these samples, in
469 comparison to the green-yellow emission (compare Fig. 2, 3 and 4 for five samples as examples).
470 Isolated centres are typically modelled in a manner whereby luminescence intensity and defect
471 concentration are proportional (e.g. Speit and Lehmann, 1976, 1982a; Finch and Klein, 1999). Fading,

472 understood as tunnelling from an electron trap to a nearby recombination centre (e.g. Visocekas,
473 1985), is dependent on the density of recombination centres in the vicinity of the electron trap
474 (Huntley, 2006). We infer that where the density of recombination centres increases, the distance
475 between the electron trap as a donor and the recombination centre as the acceptor of the tunnelling
476 electron will be smaller (Jain et al., 2012). In contrast, fewer blue recombination centres will result not
477 only in lower signal intensities, but reduces the likelihood of a blue recombination centre being within
478 tunnelling distance of an electron trap and lower fading rates will be observed.

479 Heating of samples FSM-13LH and FSM-6LH increases the blue luminescence emission intensity (Figs.
480 5 and 6), which we interpret as an increase in Al-Si disorder, populating Al-O-Al bridges and thus
481 increasing the number of blue luminescence centres. Along with the increase in blue luminescence
482 intensity, the fading rate increases (Table 4, Fig. 8B) from 0.93 ± 1.52 %/decade (FSM-13) to 3.24 ±
483 0.16 %/decade (FSM-13LH) and 2.75 ± 1.47 %/decade (FSM-6) to 4.99 ± 0.20 %/decade (FSM-6LH).
484 Another interesting observation can be made when comparing Lx/Tx values of the unheated and
485 heated samples FSM-13/FSM-13LH and FSM-6/FSM-6LH during the fading measurements (Figs. S1 A,
486 B and S2 G, H). The unheated samples show very variable Lx/Tx values between the different aliquots
487 (for instance ranging from ~2.7 to 4.7 for FSM-13, Fig. S1 A) while the heated aliquots have very
488 consistent values (~2.7 for the prompt measurement of FSM-13LH, Fig. S1 B). It is also intriguing that
489 the Lx/Tx values of the prompt measurement of the heated samples are similar to the long delay Lx/Tx
490 values of the unheated counterparts. We cannot explain these two observations, but they may
491 indicate that prolonged heating influences the luminescence sensitivity of the sample material, in a
492 way which cannot be corrected by the test dose. A further observation based on the unheated and
493 heated sample pairs is that while we observe an increase in fading of the $IRSL_{50}$ signal for the heated
494 samples (FSM-13LH and FSM-6LH) compared with their unheated counterparts (FSM-13 and FSM-6),
495 for the post-IR $IRSL_{225}$ signal there is no significant change in fading (Table 4). We conjecture that this
496 could indicate that prolonged heating increases the density of recombination centres proximal to the
497 electron trap (and this causes the increase in fading of the $IRSL_{50}$ signal and the increase in TL signal

intensity), but that the heating does not change our ability to isolate distant recombination centres to select a signal with lower fading rate. The observations described above require further investigation to be able to explain fully their implications.

Differences in fading rates are also observed for single-phase feldspars and perthites; the single-phase feldspars (CLBR, Al-I, FSM-13) show little signal loss, whereas perthites fade to varying, but significantly greater degrees. A first order model for the behaviour of a perthite is that its properties are a linear combination of the properties of the two end-members, since it is a physical intergrowth of the two end-member phases. However, this is clearly not the case. We can explain the anomalous behaviour of the intergrowths in two ways: a) the Na- and K-feldspar components of the perthites have greater disorder than the pure end-members or b) that the fading is related to the interfaces between the Na- and K-feldspar components. Hypothesis (a) is credible – we show above that increased disorder promotes fading. Furthermore, the lattice mismatch between Na- and K-feldspars increases as they become more ordered and lattice strain resists ordering (Deer et al., 2013, p. 263-264). Hence end member Na- and K-feldspar samples will have greater Al-Si order than a perthite grown under the same conditions. However, hypothesis (b) is also credible – interfaces are atypical regions which stabilise or destabilise defects and whose states of order may be locally different to the bulk feldspar. Garcia-Guinea et al. (1999) suggested that a component of the blue luminescence is related to twins. Interfaces may stabilise different defect types; two different defects that are unlikely to occur together in a random distribution in the bulk may occur in close proximity on an interface. This suggests that a single-phase solid solution may have different properties from a perthite of the same bulk composition.

To explore the two hypotheses a) and b) above, we contrast the behaviour of macroperthite and cryptoperthite. Cryptoperthites have nm-scale intergrowths and there is a greater volume of the feldspar bulk occupied by interface (Brown and Parsons, 1984b). Also, since the elastic interfacial strain in cryptoperthite is so high, one expects the Al-Si disorder to be greater in cryptoperthite

compared to a macroperthite of the same composition. However, we observe that macroperthite show greater fading rates than cryptoperthite (Fig 8, Table 4). If the state of order (hypothesis a) were the sole driving factor, the opposite would have been observed. Our conclusion is therefore that the interfaces between the Na- and K-feldspar phases are implicated in the fading of perthite. In cryptoperthite, this may be elastic strain around the interfaces at which the two different feldspar lattices are forced to remain coherent (Brown et al. 1997). Since the fading rates of cryptoperthite and macroperthite are different, we explore the differences in the morphologies of the interfaces. Boundaries between the K- and Na- feldspar phases in cryptoperthite are highly strained but fully coherent (i.e. the framework passes continuously from one phase to another, Brown et al., 1997). In macroperthite, interfaces are semi-coherent, i.e. the lattices are commonly joined across the boundary but not always, creating a region of dislocations and dangling bonds (e.g. Lee et al. 1995, Lee and Parsons, 1997; Parsons et al., 2015). Since fading is understood as the loss of charge from an electron trap to a nearby recombination centre, we hypothesise that a higher density of defects concentrated around semi-coherent interfaces in macroperthite are implicated in the higher fading rates. It may be that defect families such as regions of local disorder, dangling bonds, element substitutions etc. are all stabilised by their proximity to semi-coherent perthite interfaces, driving defects to cluster, which in turn allows direct defect-defect interactions. Interfaces are thus proposed as regions in which high defect densities result in shorter distances between donor and acceptor of a tunnelling electron (Jain et al., 2012).

Thus, we propose that fading in feldspars is not only a phenomenon of feldspars with a high-temperature (disordered) structural state, such as volcanic feldspars (e.g. Wintle, 1973; Visocekas and Zink, 1995; Visocekas et al., 2014; Guérin and Visocekas, 2015), but also related to perthite interfaces. Fading is controlled by the density of defects (Huntley, 2006) and defect clustering, which in turn is inferred to be influenced by (i) the degree of Si and Al ordering on the framework, (ii) the interfaces in perthites and (iii) elastic strain areas within the feldspar crystal. The only feldspars in this study, which show fading rates below 1 % are ordered single-phase albite and microcline. This observation

549 of very low fading rates of ordered feldspars is in good agreement with suggestions by Visocekas and
550 Zink (1995) and fading measurements on some microcline and albite specimen by Spooner (1994).

551 Our fading results show that for alkali feldspars, the structural state and the nature of interfaces within
552 the crystal are more important than chemical composition when interpreting luminescence. The
553 observation of increasing fading with increasing Al disorder on the framework is consistent with the
554 properties of plagioclase in which fading rises almost linearly with increasing concentration of Ca^{2+}
555 (Huntley and Lian 2006; Huntley et al. 2007) since Ca^{2+} substitution on the M-site is offset by increases
556 in the Al content of the lattice and therefore Al-O-Al populations are dependent on Ca content.

557 Due to exsolution of feldspar during cooling in plutonic rocks (e.g. granite), most alkali feldspars in
558 rocks and unconsolidated sediments are perthites (e.g. Deer et al., 2013). Unfortunately, perthites
559 faded in our experiments. The feldspars extracted from unconsolidated sediments (WHB-7 and HAM-
560 5) and from crushed bedrock material used in luminescence thermochronometry (MBT-I-2430) in this
561 study exhibit fading rates of the $IRSL_{50}$ signal within the range seen for cryptoperthites in this study
562 (Table 4, Fig. 8B). A similarity in fading rates and in TL emission spectra of sediment and
563 thermochronometry samples and perthite is consistent with similar mechanisms playing a role in
564 these sets of samples. The similarities hint that in feldspar grains extracted from sediment and rocks
565 for optical dating and thermochronometry, Al-Si order, interface morphology and elastic strain are
566 implicated both in the blue emission and in the fading rate.

567 **6 Conclusions**

568 The present study analyses the effects of chemistry, the number of phases present within a single
569 crystal and the relative degree of framework disorder on TL emission spectra and fading rates of alkali
570 feldspars. The investigated sample suite includes Na- and K-feldspar end members, perthites with K-
571 and Na-feldspar lamellae on different scales, as well as material routinely used in luminescence dating
572 studies and luminescence thermochronometry. We observed variations in the intensity of the blue
573 luminescence emission and the rate of anomalous fading of the IRSL signal in our feldspars. We

associate the blue luminescence with the blue recombination centre being located on an Al-O-Al bridge. The blue luminescence intensity increases as a function of the population of Al-O-Al bridges which increases with Al-Si disorder. Ordered, single-phase feldspars, such as albite and microcline, show very little fading, whereas the variations in fading rates in perthites are suggested to be linked to a) the degree of Si and Al order on the framework and b) defect clustering associated with semi-coherent perthite interfaces which modify the intensity of the blue emission and the extent to which this emission fades.

Our study highlights the importance of detailed mineralogical characterisation of feldspar samples in order to understand the complex drivers behind the variability seen in the blue luminescence intensity and anomalous fading rates of the IRSL signal. This paper combines information on sample chemistry, structural state, phases present, luminescence emissions and anomalous fading rate of alkali feldspar. From these data we are able to differentiate between very low fading single-phase end members and perthitic feldspars which all fade. Interestingly, the same differentiation can be made from TL emission spectra, where single-phase feldspars show a more intense yellow-green emission, compared to the blue emission, while perthites show the opposite, with the blue emission being dominant. Perhaps it would be possible to identify those feldspar grains which are single phase (and hence likely to have a low fading rate) by looking for those with a high value for the ratio of the yellow-green to blue emission. Such measurements could be routinely feasible using automated filter changers in combination with an EMCCD camera, and may avoid the need for costly and time consuming chemical and structural analyses of individual grains.

Acknowledgements

SR would like to thank Aberystwyth University for funding her PhD research through an AberDoc PhD scholarship (Aberystwyth University). Sample WHB-7 was taken during a field campaign in May 2018, which was made possible by a RGS-IBG postgraduate research grant awarded to SR. Sample HAM-5 was taken in the framework of the QuakeRecNankai project, funded by the Belgian Science Policy

599 Office (BELSPO BRAIN-be BR/121/A2). We thank Dr Javier Garcia-Guinea for CLBR and Dr Renske
600 Lambert for MBT-I-2430. The authors would like to thank Prof Mike Henderson (Manchester
601 University) for facilitating the introduction between some of the authors. SR would like to thank
602 Karsten Bracht-Nielsen (Technical University of Denmark) for technical support with the Andor
603 Spectrometer, and Andrew Brown (Aberystwyth University) for laboratory assistance during the
604 heating experiments. We would like to thank three anonymous referees for their constructive
605 comments, which improved the manuscript.

606 **References**

607 Baril, M.R., 2004. CCD imaging of the infra-red stimulated luminescence of feldspar. Radiation
608 Measurements 38, 81-86.

609 Brown, W.L., Parsons, I., 1984a. The nature of potassium feldspar, exsolution microtextures and
610 development of dislocations as a function of composition in perthitic alkali feldspars. Contributions to
611 Mineralogy and Petrology 86, 335-341.

612 Brown, W.L., Parsons, I., 1984b. Exsolution and coarsening mechanisms and kinetics in an ordered
613 cryptoperthites series. Contributions to Mineralogy and Petrology 86, 3-18.

614 Brown, W.L., Lee, M.R., Waldron, K.A., Parsons, I., 1997. Strain-driven disordering of low microcline to
615 low sanidine during partial phase separation in microperthites. Contributions to Mineralogy and
616 Petrology 127, 305-313.

617 Bussy, F., Von Raumer, J.F., 1993. U-Pb dating of Palaeozoic events in the Mont-Blanc crystalline
618 massif, western Alps. Terra. Nova Abstracts 5, 382.

619 Bussy, F., Schaeltegger, U., Marro, C., 1989. The age of the Mont Blanc granite (western Alps): a
620 heterogenous isotopic system dated by Rb-Sr whole rock determination on its microgranular enclaves.
621 Schweizer Mineralogische und Petrologische Mitteilungen 69, 3–13.

622 Buylaert, J.-P., Jain, M., Murray, A.S., Thomsen, K.J., Thiel, C., Sohbati, R., 2012. A robust feldspar
623 luminescence dating method for Middle and Late Pleistocene sediments. Boreas 41, 435-451.

624 Cassadanne, J.P., Roditi, M., 1996. The location, geology and mineralogy of gem tourmalines in Brazil.
625 Journal of Gemmology 25 (4), 263–298.

626 Correcher, V., Garcia-Guinea, J., Delago, A., 2000. Influence of preheating treatment on the
627 luminescence properties of adularia feldspar ($KAlSi_3O_8$). Radiation Measurements 32, 709-715.

628 Cunningham, G.J., 1981. Petrology and geochemistry of Lewisian pegmatites and granites, N.W.,
629 Scotland. PhD thesis, Imperial Collage London, United Kingdom.

630 Deer, W.A., Howie, R.A., Zussman, J., 2013. An introduction to the rock-forming minerals. Third
631 Edition. Mineralogical Society of Great Britain and Ireland.

632 Duller, G.A.T., 2015. The Analyst software package for luminescence data: overview and recent
633 improvements. Ancient TL 33, 35-42.

634 Finch, A.A., Klein, J., 1999. The causes and petrological significance of cathodoluminescence emissions
635 from alkali feldspars. Contributions to Mineralogy and Petrology 135, 234-243.

636 Garcia-Guinea, J., Rendell, H.M., Sanchez-Muñoz, L., 1996. Luminescence spectra of alkali feldspars:
637 some relationships between structural features and luminescence emission. Radiation Protection
638 Dosimetry 66, 395-398.

639 Garcia-Guinea, J., Townsend, P.D., Sanchez-Muños, L.., Rojo, J.M., 1999. Ultraviolet-blue ionic
640 luminescence of alkali feldspars from bulk and interfaces. Physics and Chemistry of Minerals 26, 658-
641 667.

642 Geake, J.E., Walker, G., Mills, A.A., Garlick, G.F.J., 1971. Luminescence of Apollo lunar samples.
643 Proceedings of the Second Lunar Science Conference 3, 2265-2275.

644 Govindaraju, K., 1995. Update (1984-1995) on two GIT-IWG geochemical reference samples: Albite
645 from Italy, Al-I and iron formation sample from Greenland, IF-G. Geostandards Newsletter 19, 55-96.

646 Guérin, G., Visocekas, R., 2015. Volcanic feldspars anomalous fading: Evidence for two different
647 mechanisms. Radiation Measurements 81, 218-223.

648 Harrison, T.N., Parsons, I., Brown, P.E., 1990. Mineralogical evolution of fayalite-bearing rapakivi
649 granites from the Prins Christians Sund pluton, South Greenland. Mineralogical Magazine 54, 57–66.

650 Huntley, D.J., Lamothe, M., 2001. Ubiquity of anomalous fading in K-feldspars and the measurement
651 and correction for it in optical dating. Canadian Journal of Earth Sciences 38, 1093-1106.

652 Huntley, D.J., 2006. An explanation of the power-law decay of luminescence. Journal of Physics:
653 Condensed Matter 18, 1359-1365.

654 Huntley, D.J., Lian, O.B., 2006. Some observations on tunnelling of trapped electrons in feldspars and
655 their implications for optical dating. Quaternary Science Reviews 25, 2503-2512.

656 Huntley, D.J., Baril, M.R., Haider, S., 2007. Tunnelling in plagioclase feldspars. Journal of Physics D:
657 Applied Physics 40, 900-906.

658 Jain, M., Guralnik, B., Andersen, M. T., 2012. Stimulated luminescence emission from localized
659 recombination in randomly distributed defects. Journal of Physics: Condensed Matter 24, 385402.

660 Jenkins, G.T.H., Duller, G.A.T., Roberts, H.M., Chiverrell, R.C., Glasser, N.F., 2018. A new approach for
661 luminescence dating glaciofluvial deposits – High precision optical dating of cobbles. Quaternary
662 Science Reviews 192, 263-273.

663 Kars, R.H., Wallinga, J., Cohen, K.M., 2008. A new approach towards anomalous fading correction for
664 feldspar IRSL dating – tests on samples in field saturation. Radiation Measurements 43, 786-790.

665 King, G.E., Herman, F., Guralnik, B., 2016. Northward migration of the eastern Himalayan syntaxis
666 revealed by OSL thermochronometry. Science 353, 800-804.

667 Kook, M.H., Lapp, T., Murray, A.S., Thiel, C., 2012. A Risø XRF Attachment for Major Element Analysis
668 of Aliquots of Quartz and Feldspar Separates. UK Luminescence and ESR Meeting, Aberystwyth, pp.
669 37 September 2012 (abstract).

670 Krbetschek, M.R., Gütze, J., Dietrich, A., Trautmann, T., 1997. Spectral information from minerals
671 relevant for luminescence dating. Radiation Measurements 27, 695-748.

672 Lapp, T., Kook, M., Murray, A.S., Thomsen, K.J., Buylaert, J.-P., Jain, M., 2015. A new luminescence
673 detection and stimulation head for the Risø TL/OSL reader. Radiation Measurements 81, 178-184.

674 Lee, M.R., Waldron, K.A., Parsons, I., 1995. Exsolution and alteration microtextures in alkali feldspar
675 phenocrysts from the Shap granite. Mineralogical Magazine 59, 63-78.

676 Lee, M.R., Parsons, I., 1997. Dislocation formation and albitization in alkali feldspars from the Shap
677 Granite. Mineralogical Magazine 82, 557-570.

678 Li, B., Li, S.-H., 2011. Thermal stability of infrared stimulated luminescence of sedimentary K-feldspar.
679 Radiation Measurements 46, 29-36.

680 Neudorf, C.M., Roberts, R.G., Jacobs, Z., 2012. Sources of overdispersion in a K-rich feldspar sample
681 from north-central India: Insights from De, K content and IRSL age distributions for individual grains.
682 Radiation Measurements 47, 696-702.

683 Parsons, I., 1978. Feldspars and fluids in cooling plutons. Mineralogical Magazine 42, 1-17.

684 Parsons, I., Thompson, P., Lee, M.R., Cayzer, N., 2005. Alkali feldspar microtextures as provenance
685 indicators in siliclastic rocks and their role in feldspar dissolution during transport and diagenesis.
686 Journal of Sedimentary Research 75, 921-942.

687 Parsons, I., 2010. Feldspars defined and described: a pair of posters published by the Mineralogical
688 Society. Sources and supporting information. Mineralogical Magazine, 74(3), 529-551.

689 Parsons, I., FitzGerald, J.D., Lee, M.R., 2015. Routine characterization and interpretation of complex
690 alkali feldspar intergrowth. American Mineralogist 100, 1277-1303.

691 Polymeris, G.S., Theodosoglou, E., Kitis, G., Tsirliganis, N.C., Koroneos, A., Paraskevopoulos, K.M.,
692 2013. Preliminary results on structural state characterization of K-feldspars by using
693 thermoluminescence. Mediterranean Archaeology and Archaeometry 13, 155-161.

694 Prasad, A.K., Lapp, T., Kook, M., Jain, M., 2016. Probing luminescence centres in Na rich feldspars.
695 Radiation Measurements 90, 292-297.

696 Prasad, A.K., 2017. Understanding defect related luminescence processes in wide bandgap materials
697 using low temperature multi-spectroscopic techniques. PhD Thesis, Technical University of Denmark,
698 196 p.

699 Reimann, T., Thomsen, K.J., Jain, M., Murray, A.S., Frechen, M., 2012. Single-grain dating of young
700 sediments using the pIRIR signal from feldspar. Quaternary Geochronology 11, 28-41.

701 Rendell, H.M., Clarke, M.L., 1997. Thermoluminescence, radioluminescence and
702 cathodoluminescence spectra of alkali feldspars. Radiation Measurements 27, 263-272.

703 Riedesel, S., Brill, D., Roberts, H.M., Duller, G.A.T., Garrett, E., Zander, A.M., King, G.E., Tamura, T.,
704 Burow, C., Cunningham, A., Seeliger, M., De Batist, M., Heyvaert, V.M.A., Fujiwara, O., Brückner, H.
705 and the QuakeRecNankai Team, 2018. Single-grain luminescence chronology of historical extreme-
706 wave event deposits recorded in a coastal lowland, Pacific coast of central Japan. Quaternary
707 Geochronology 45, 37–49.

708 Riedesel, S., King, G.E., Prasad, A.K., Kumar, R., Finch, A.A., Jain, M., 2019. Optical determination of
709 the width of the band-tail states, and the excited and ground state energies of the principal dosimetric
710 trap in feldspar. Radiation Measurements 125, 40-51.

Şahiner, E., Kitis, G., Pagonis, V., Meriç, N., Polymeris, G.S., 2017. Tunnelling recombination in conventional, post-inrared and post-infrared multi-elevated temperature IRSL signals in microcline feldspar. Journal of Luminescence 188, 514-523.

Sanderson, D.C.W., 1988. Fading of thermoluminescence in feldspars: Characteristics and corrections. Nuclear Tracks and Radiation Measurements 14, 155-161.

Smedley, R.K., Glasser, N.F., Duller, G.A.T., 2016. Luminescence dating of glacial advances at Lago Buenos Aires (~46°S), Patagonia. Quaternary Science Reviews 134, 59-73.

Speit, B., Lehmann, G., 1976. Hole centers in the feldspar sanidine. Physica Status Solidi 36, 471-481.

Speit, B., Lehmann, G., 1982a. Radiation Defects in Feldspars. Physics and Chemistry of Minerals 8, 77-82.

Speit, B., Lehmann, G., 1982b. A comparative study of thermoluminescence and isothermal destruction of radiation defects in feldspars. Journal of Luminescence 27, 127-136.

Spooner, N.A., 1992. Optical dating: Preliminary results on the anomalous fading of luminescence from feldspars. Quaternary Science Reviews 11, 139-145.

Spooner, N.A., 1994. The anomalous fading of infrared-stimulated luminescence from feldspars. Radiation Measurements 23, 625-632.

Stevens, T., Buylaert, J.-P., Thiel, C., Ujavri, G., Yi, S., Murray, A.S., Frechen, M., 2018. Ice-volume-forced erosion of the Chinese Loess Plateau global Quaternary stratotype site. Nature Communications 9: 983.

Telfer, D.J., Walker, G., 1978. Ligand field bands of Mn^{2+} and Fe^{3+} luminescence centres and their site occupancy in plagioclase feldspars. Modern Geology 6, 199-210.

Templer, R.H., 1986. The localised transition model of anomalous fading. Radiation Protection Dosimetry 17, 493-497.

734 Thiel, C., Buylaert, J.-P., Murray, A.S., Terhorst, B., Hofer, I., Tsukamoto, S., Frechen, M., 2011.
735 Luminescence dating of the Stratzing loess profile (Austria) – Testing the potential of an elevated
736 temperature post-IR IRSL protocol. Quaternary International 234, 23-31.

737 Thomsen, K.J., Murray, A.S., Jain, M., Bøtter-Jensen, L., 2008. Laboratory fading rates of various
738 luminescence signals from feldspar-rich sediment extracts. Radiation Measurements 43, 1474-1486.

739 Trauerstein, M., Lowick, S., Preusser, F., Rufer, D., Schlunegger, F., 2012. Exploring fading in single
740 grain feldspar IRSL measurements. Quaternary Geochronology 10, 327-333.

741 Ussher, W.A.E., Barrow, G., McAlister, D.A., 1909. The Geology of the country around Bodmin and St.
742 Austell. Memoirs of the Geological Survey England and Wales – Explanation of Sheet 347.

743 Valla, P.G., Lowick, S.E., Herman, F., Champagnac, J.-D., Steer, P., Guralnik, B., 2016. Exploring IRSL50
744 fading variability in bedrock feldspars and implications for OSL thermochronometry. Quaternary
745 Geochronology 36, 55-66.

746 Visocekas, R., 1985. Tunnelling radiative recombination on labradorite: Its association with anomalous
747 fading of thermoluminescence. Nuclear Tracks and Radiation Measurements 10, 521-529.

748 Visocekas, R., Zink, A., 1995. Tunneling afterglow and point defects in feldspars. Radiation Effects and
749 Defects in Solids 134, 265-272.

750 Visocekas, R., Zink, A., 1999. Use of the red TL emission band of alkali feldspars for dosimetry and
751 dating. Quaternary Geochronology 18, 271-278.

752 Visocekas, R., Barthou, C., Blanc, P., 2014. Thermal quenching of far-red Fe3+ thermoluminescence of
753 volcanic K-feldspars. Radiation Measurements 61. 52-73.

754 Wintle, A.G., 1973. Anomalous fading of thermoluminescence in mineral samples. Nature 245, 143-
755 144.

Wintle, A.G., 1977. Detailed study of a thermoluminescent mineral exhibiting anomalous fading. Journal of Luminescence 15, 385-393.

Xiao, Y., Kirkpatrick, J., Hay, R.L., Kim, Y.J., Phillips, B.L., 1995. Investigation of Al,Si order in K-feldspars using ^{27}Al and ^{29}Si MAS NMR. Mineralogical Magazine 59, 47-61.

Table 1. Details regarding the origin, chemical composition, phases and size of perthite lamella for samples investigated. The chemical composition in % feldspars, was done using stoichiometric conversion of the semi-quantitative XRF data. Chemical composition and present phases of R1-11A was taken from Harrison et al. (1990). Present phases are based on semi-quantitative XRD analyses.

Sample ID	Origin	Chemical composition (FS %)			Phases						Extent of perthite development	Reference
		K-FS	Na-FS	Ca-FS	Microcline	Orthoclase	Sanidine	Albite	Anorthite	Other		
FSM-13	Brazil	98.5	1.5	0.0	100.0	-	-	-	-	-	none	-
FSM-13LH	Brazil	98.5	1.5	0.0	100.0	-	-	-	-	-	none	-
FSM-3	Granite pegmatite, Toe Head, South Harris, Scotland, UK (Cunningham, 1981)	82.5	17.2	0.3	78.0	-	-	22.0	-	-	cryptoperthites	-
R1-11A	Rapakivi Granite, South Greenland	81.0	19.0	1.0	Microcline and albite (Harrison et al., 1990)						cryptoperthite	Harrison et al., 1990; Finch and Klein, 1999; Riedesel et al., 2019
FSM-15	Buckingham, Quebec, Canada	80.4	19.6	0.0	82.0	-	-	18.0	-	-	cryptoperthite	-
FSM-14	Iveland, Southern Norway	78.3	21.2	0.5	54.0	-	-	46.0	-	-	cryptoperthite	-
FSM-8	Norway	77.1	22.6	0.3	68.0	-	-	32.0	-		cryptoperthite	-
FSM-7	Unknown	76.8	22.0	1.2	48.0	-	-	51.0	-	1.0	cryptoperthite	-
FSM-5	Unknown	74.8	25.20	0.0	57.0	-	-	43.0	-	-	Macroperthite	-
FSM-6	Granite pegmatite, Trezaise Quarry, Cornwall, UK (see Ussher et al., 1909)	74.4	25.3	0.3	-	38.0	-	62.0	-	-	cryptoperthite	-
FSM-6LH	Trezaise Quarry, Cornwall, UK	74.4	25.3	0.3	-	-	100.0	-	-	-	none	-
FSM-11	Perth, Canada	65.2	34.8	0.0	62.0	-	-	38.0	-	-	macroperthite	-
Al-I	Pinzele, Trente, Italy (Govindaraju, 1995)	1.0	97.0	2.0	-	-	-	-	-	-	none	-
CLBR	Pegmatite, Golonca District, Minas Gerais, Brazil (Cassadanne and Roditi, 1996)	0.5	99.3	0.2	-	-	-	100	-	-	none	Rendell and Clarke (1997); Garcia-Guinea et al., 1999; Riedesel et al., 2019

Table 2. Details on feldspar extracted from sediment and bedrock samples. The chemical composition in % feldspars, was done using stoichiometric conversion of the semi-quantitative XRF data. Present phases are based on semi-quantitative XRD analyses.

Sample ID	Origin	Chemical composition (FS %)			Phases						Size of perthite lamella	Reference
		K-FS	Na-FS	Ca-FS	Microcline	Orthoclase	Sanidine	Albite	Anorthite	Other		
MBT-I-2430	Calc-alkaline granite, Mont Blanc, Italy (Bussy et al., 1989; Bussy and Von Raumer, 1993)	86.1	13.4	0.6	85.0	-	-	15.0	-	-	-	Lambert, 2018; Riedesel et al., 2019
HAM-5	Lake Hamana, Japan	70.4	27.2	2.4	-	30.0	-	27.0	-	43.0	-	Riedesel et al. 2019
WHB-7	Channelled Scablands, Washington State, USA	63.9	31.5	4.6	37.0	-	-	30.0	-	33.0	-	-

Table 3. Post-$IR_{50}IRSL_{225}$ protocol used for the determination of fading rates.

Step	Details	Obtained
1	Beta dose ~90 Gy	
2	Preheat for 60 s at 250 °C	
3	IR stimulation at 50 °C for 200 s ($IRSL_{50}$)	Lx_1 ($IRSL_{50}$)
4	IR stimulation at 225 °C for 300 s (post-IR $IRSL_{225}$)	Lx_2 (post-$IR_{50}IRSL_{225}$)
5	Beta dose ~30 Gy	
6	Preheat for 60 s at 250 °C	
7	IR stimulation at 50 °C for 200 s ($IRSL_{50}$)	Tx_1 ($IRSL_{50}$)
8	IR stimulation at 225 °C for 300 s (post-IR $IRSL_{225}$)	Tx_2 (post-$IR_{50}IRSL_{225}$)

Table 4. Fading rates for the two luminescence signals recorded using a post-IR_{50} $IRSL_{225}$ protocol. The samples were preheated to 250 °C for 60 s, prior to IRSL measurements.

Group	Sample ID	Fading rate (g2days, %/decade)	
		$IRSL_{50}$	Post-IR $IRSL_{225}$
Single phase			
	Al-I	0.58 ± 0.30	0.29 ± 0.24
	CLBR	0.36 ± 0.60	-0.08 ± 0.37
	FSM-13	0.93 ± 1.52	0.54 ± 1.10
Macroperthites			
	FSM-5	8.99 ± 1.82	2.74 ± 0.60
	FSM-11	12.42 ± 1.71	4.07 ± 1.39
Cryptoperthites			
	FSM-3	5.71 ± 0.12	2.19 ± 0.49
	R1-11A	6.72 ± 2.51	1.86 ± 1.39
	FSM-15	4.97 ± 1.98	0.79 ± 1.73
	FSM-14	3.51 ± 1.35	1.48 ± 1.63
	FSM-8	1.80 ± 0.32	1.23 ± 1.86
	FSM-7	4.13 ± 0.46	0.55 ± 0.38
	FSM-6	2.75 ± 1.47	1.47 ± 0.97
Artificially disordered			
	FSM-13LH	3.24 ± 0.16	-0.06 ± 0.13
	FSM-6LH	4.99 ± 0.20	1.68 ± 0.13
Sediments/rocks			
	HAM-5	1.86 ± 0.46	-1.01 ± 0.20
	WHB-7	3.07 ± 0.74	1.01 ± 0.26
	MBT-I-2430	3.28 ± 0.14	1.35 ± 0.30

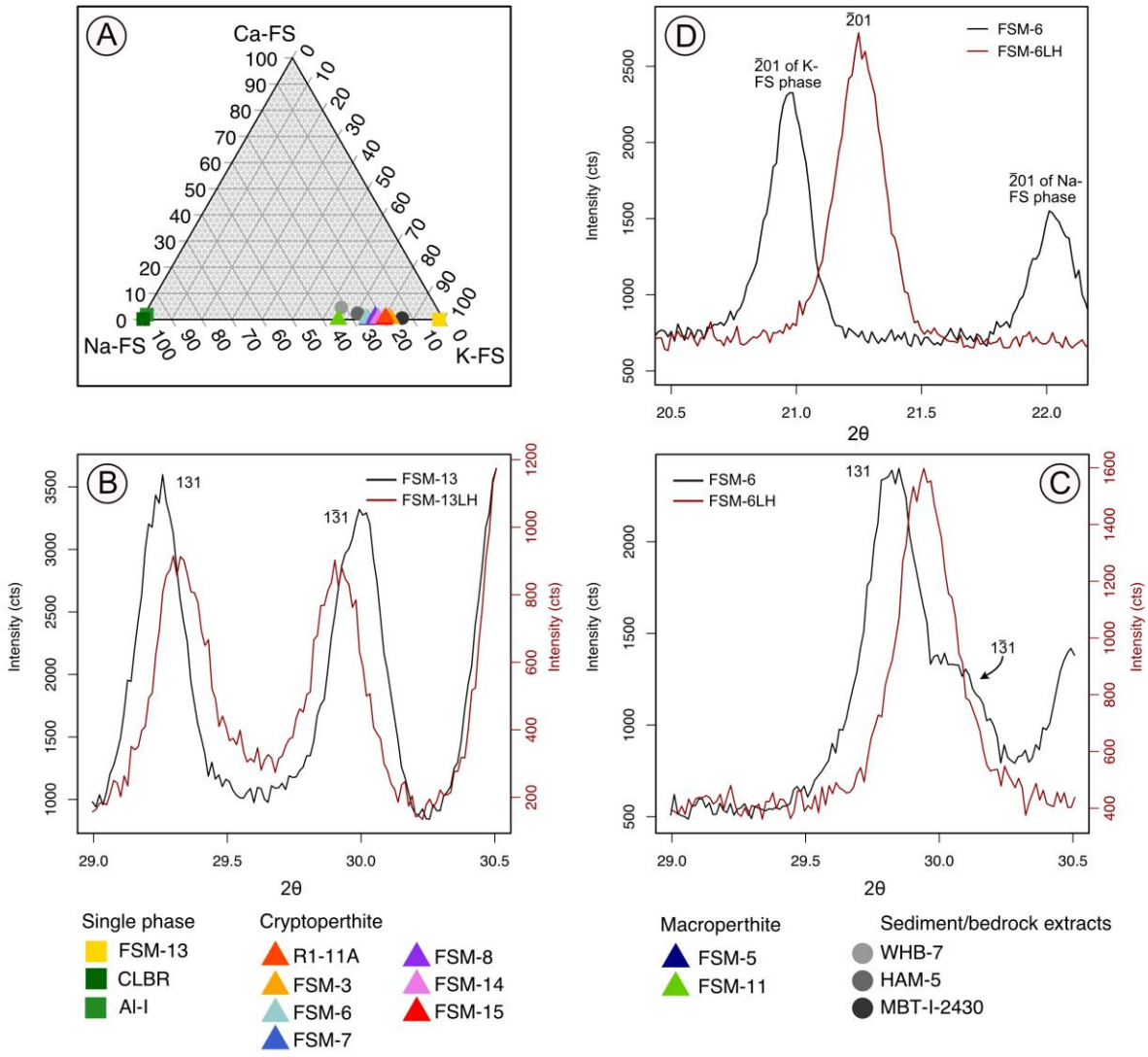

Fig. 1. A) Relative feldspar composition (%) of the samples. The relative compositions of K-, Na- and Ca-feldspar were calculated using stoichiometric conversion of XRF results. B) X-ray diffraction pattern of FSM-13 (black line) and FSM-13LH (red line) in the range of 29.0° 2θ to 30.5° 2θ. Visible are the (131) and ($1\bar{3}1$) diffraction maxima. These two diffraction maxima move closer together due to the heating of the sample material. C) X-ray diffraction pattern of FSM-6 (black line) and FSM-6LH (red line) in the range of 29.0° 2θ to 30.5° 2θ. For FSM-6 (black line) a prominent (131) diffraction maxima is visible in the figure, and in addition a minor peak, which is the remainder of the ($1\bar{3}1$) diffraction peak. After heating and rapidly cooling, only a single (131) diffraction peak remains in FSM-6LH (red line). This indicates that the original material of FSM-13 (black line in B) is more ordered than the starting material of FSM-6 (black line in C). For both samples, the X-ray diffraction pattern indicate the success of the heating experiment, as both samples are slightly more disordered than their starting material. However, it is expected that FSM-6LH is relatively more disordered than FSM-13LH. D) Comparison of the $\bar{2}01$ diffraction peak in perthite FSM-6 and in sanidine FSM-6LH. The heating experiment caused a homogenisation of the distribution of K^+ and Na^+ ions within the crystal. Whilst FSM-6 shows two $\bar{2}01$ diffraction peaks (on for each phase), FSM-6LH only shows a single diffraction peak, reflecting the homogeneous distribution of the cations. Radiation used in XRD analysis was Cu Kα.

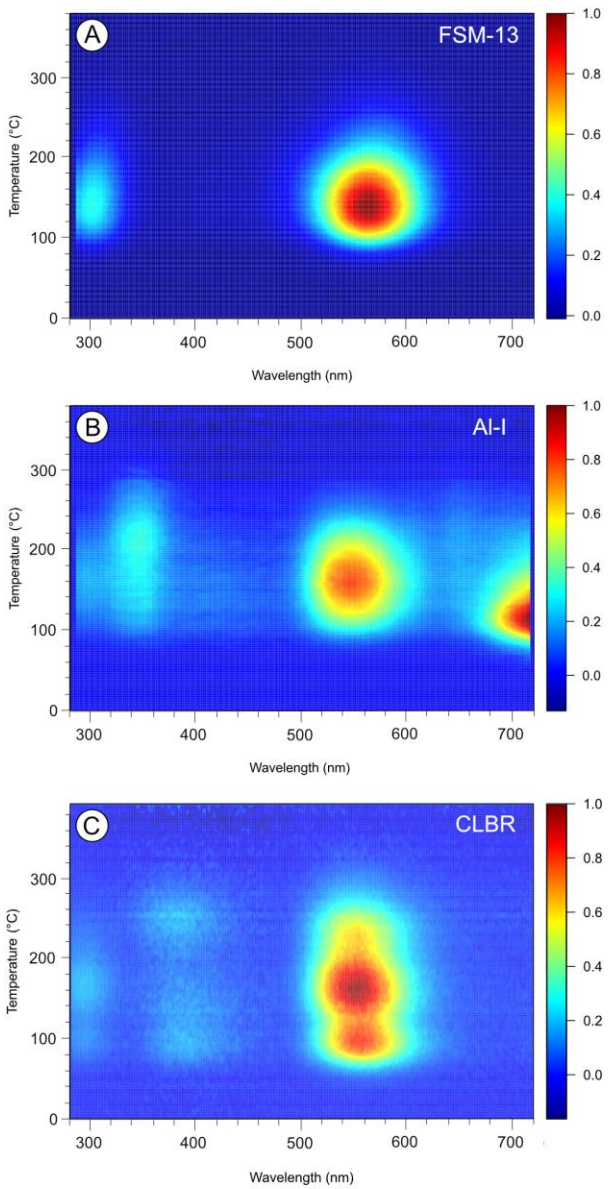

Fig. 2. TL emission spectra recorded up to 380 °C, from 280 to 720 nm. The samples shown in this figure are single-phase feldspar. FSM-13 is a microcline (A) and Al-I (B) and CLBR (C) are albite, with Al-I containing 5 % quartz. The TL intensities are normalised to the data point with the highest intensity.

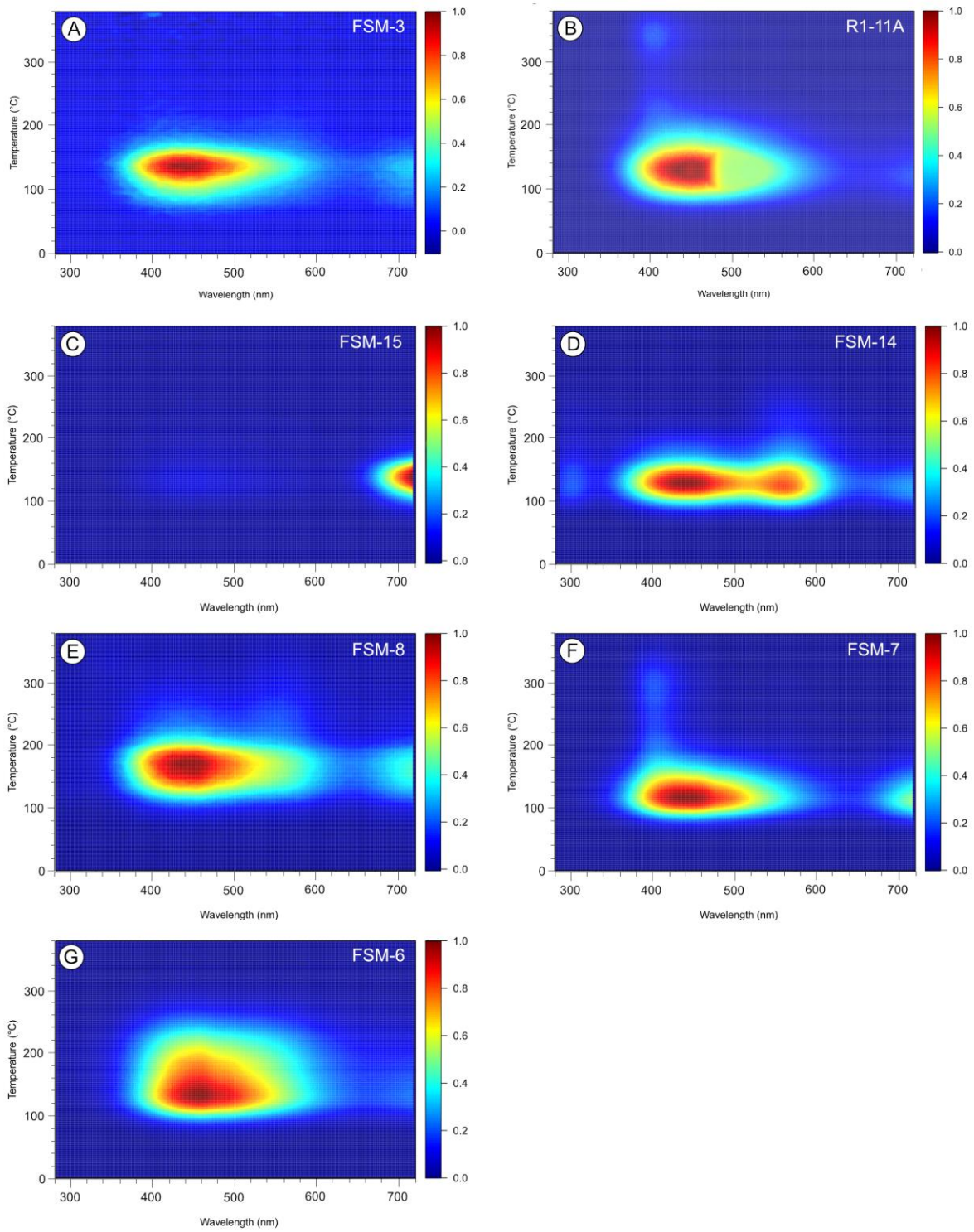

Fig. 3. TL emission spectra recorded up to 380 °C, from 280 to 720 nm. The samples shown in this figure are cryptoperthite: FSM-15 (C) is the only sample of the displayed samples, where Fe was detected during the XRF measurements. All samples consist of microcline and albite (A-F), except for FSM-6 (G), which consists of orthoclase and albite. The TL intensities are normalised to the data point with the highest intensity.

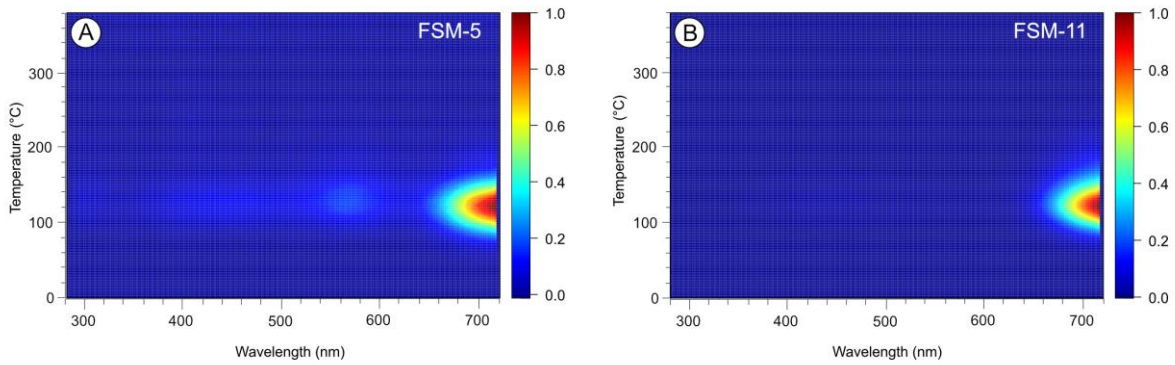

Fig. 4. TL emission spectra of perthites with coarse perthite lamella, visible with the naked eye: macroperthite. FSM-5 (A) is an amazonite sample, which shows twinning in the albite phase. XRF-measurements showed the presence of Fe in FSM-11 (B), which also is of orange colour in the microcline phase. The TL intensities are normalised to the data point with the highest intensity.

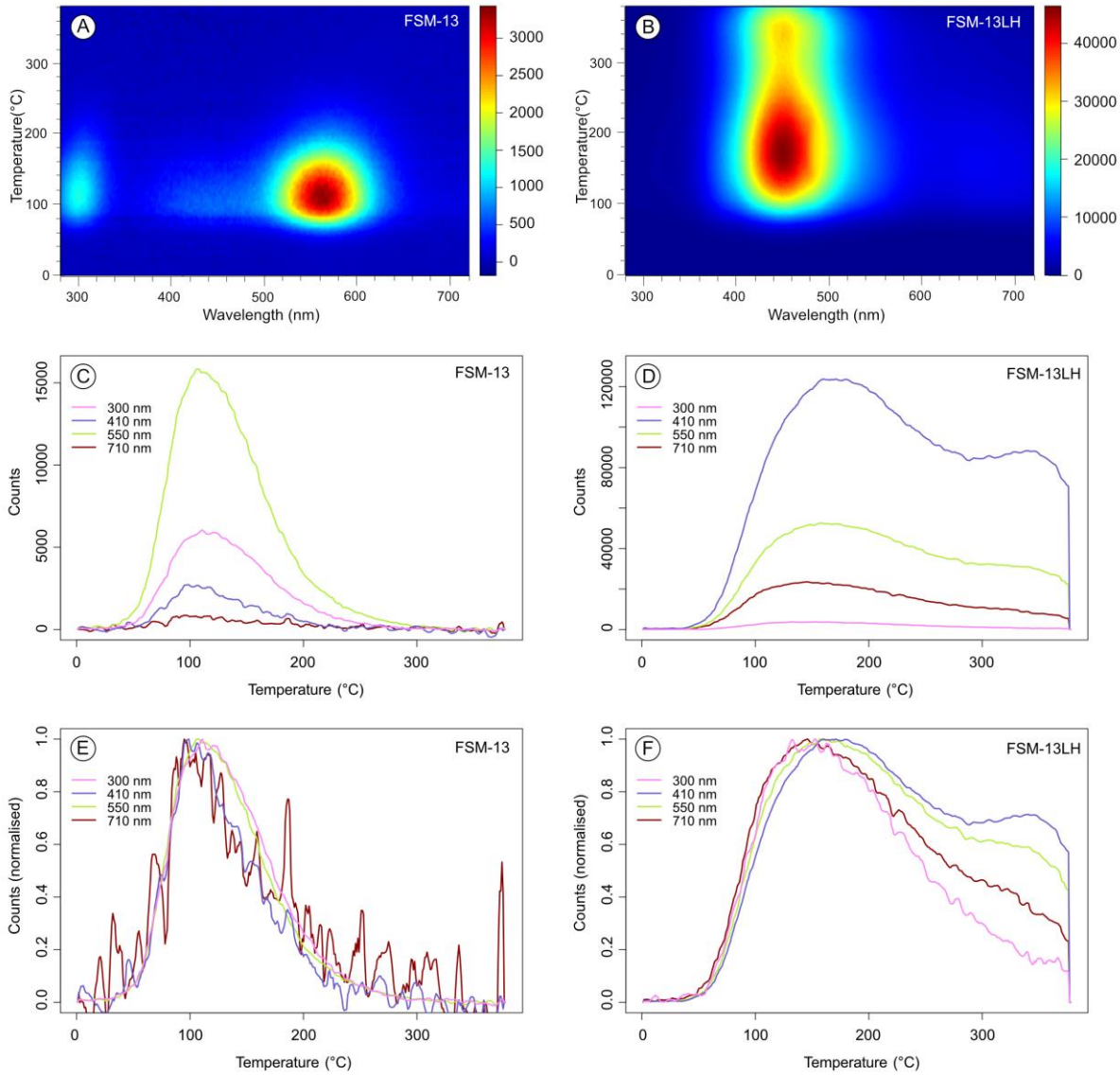

Fig. 5. Effect of heating sample FSM-13 (single phase microcline) at 1050 °C for 10 days. (A) TL spectra of the unheated material of FSM-13, (B) TL spectra of the heated fraction. (C) and (D) show the TL curve extracted from the TL spectra for different wavelengths for FSM-13 and FSM-13LH, respectively. (E) and (F) show the same data as (C) and (D), but normalised to the highest intensity for each TL curve. The measured intensities are absolute intensities in counts/0.4 nm/°C. For these measurements the same mass of sample material was used and the samples were measured during the same measurement sequence.

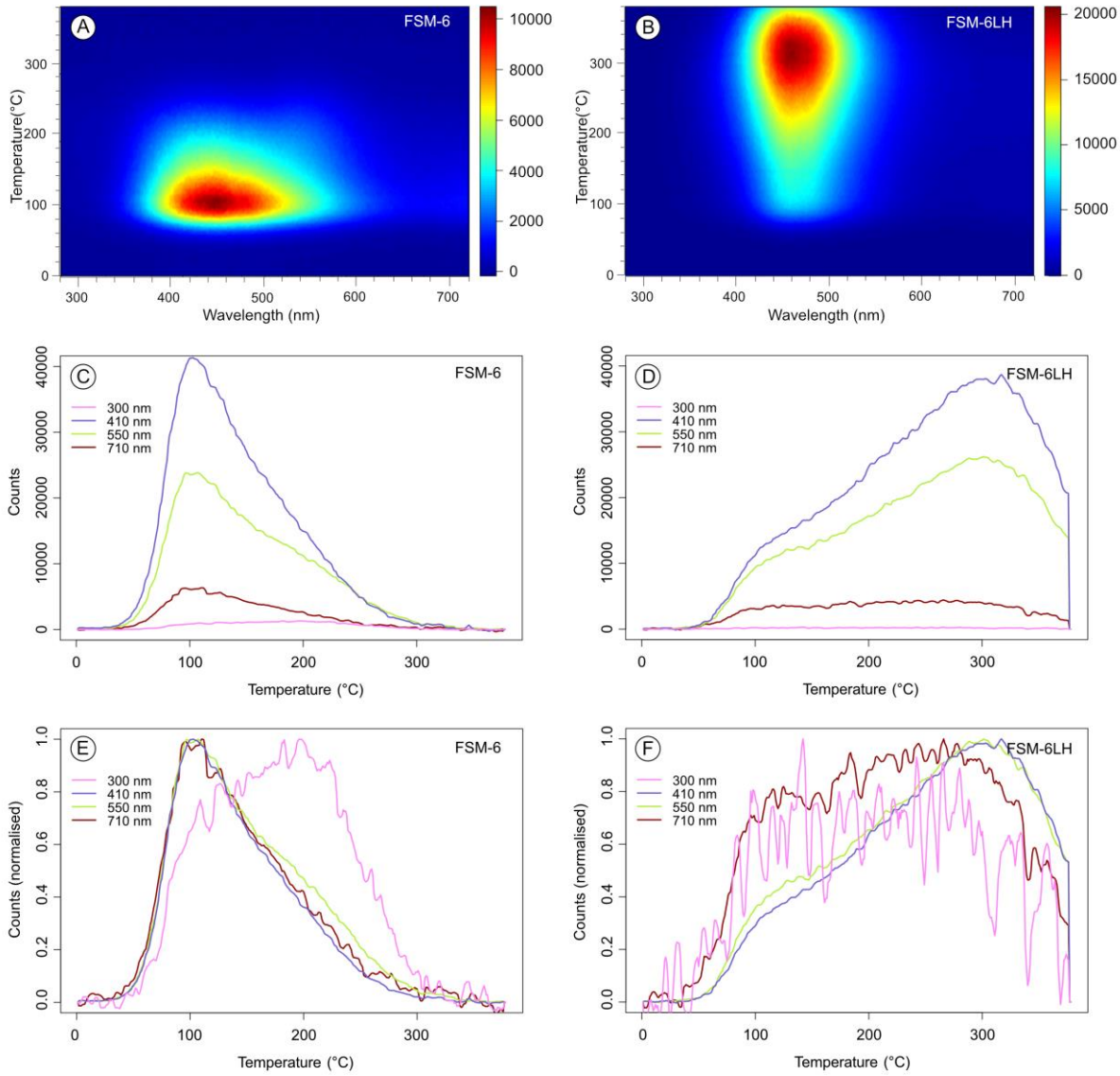

Fig. 6. Effect of heating sample FSM-6 (orthoclase and albite) at 1050 °C for 10 days. (A) TL spectra of the unheated material of FSM-6, (B) TL spectra of the heated fraction. (C) and (D) show the TL curve extracted from the TL spectra for different wavelengths for FSM-6 and FSM-6LH, respectively. (E) and (F) show the same data as (C) and (D), but normalised to the highest intensity for each TL curve. The measured intensities are absolute intensities (in cts/0.4 nm/°C). For these measurements the same mass of sample material was used and the samples were measured during the same measurement sequence.

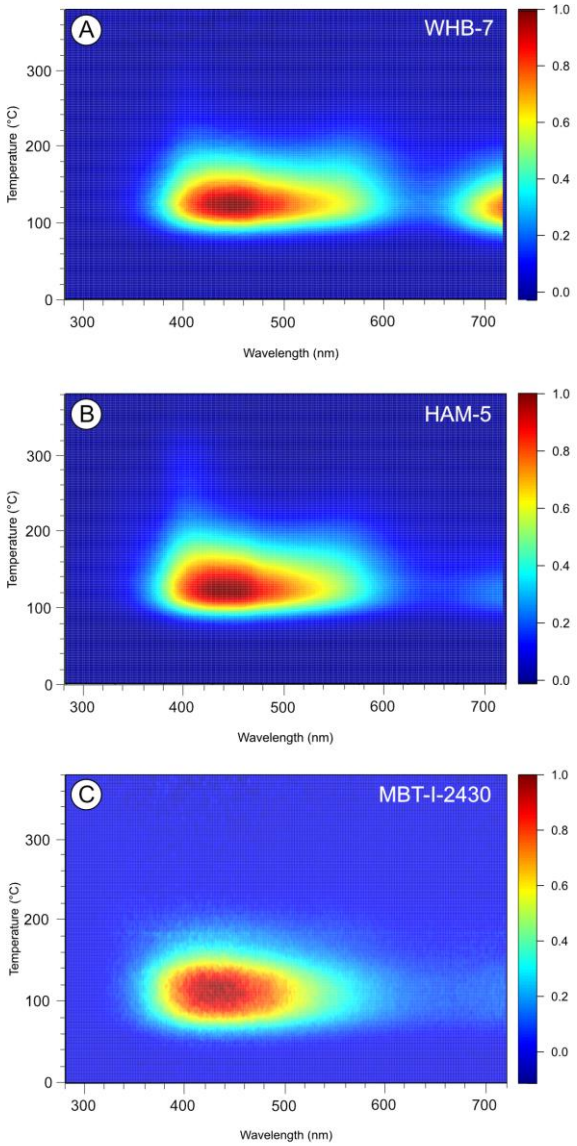

Fig. 7. TL emission spectra of alkali feldspars extracted from sediments (WHB-7, HAM-5) and bedrock (MBT-I-2430). The TL intensities are normalised to the data point with the highest intensity.

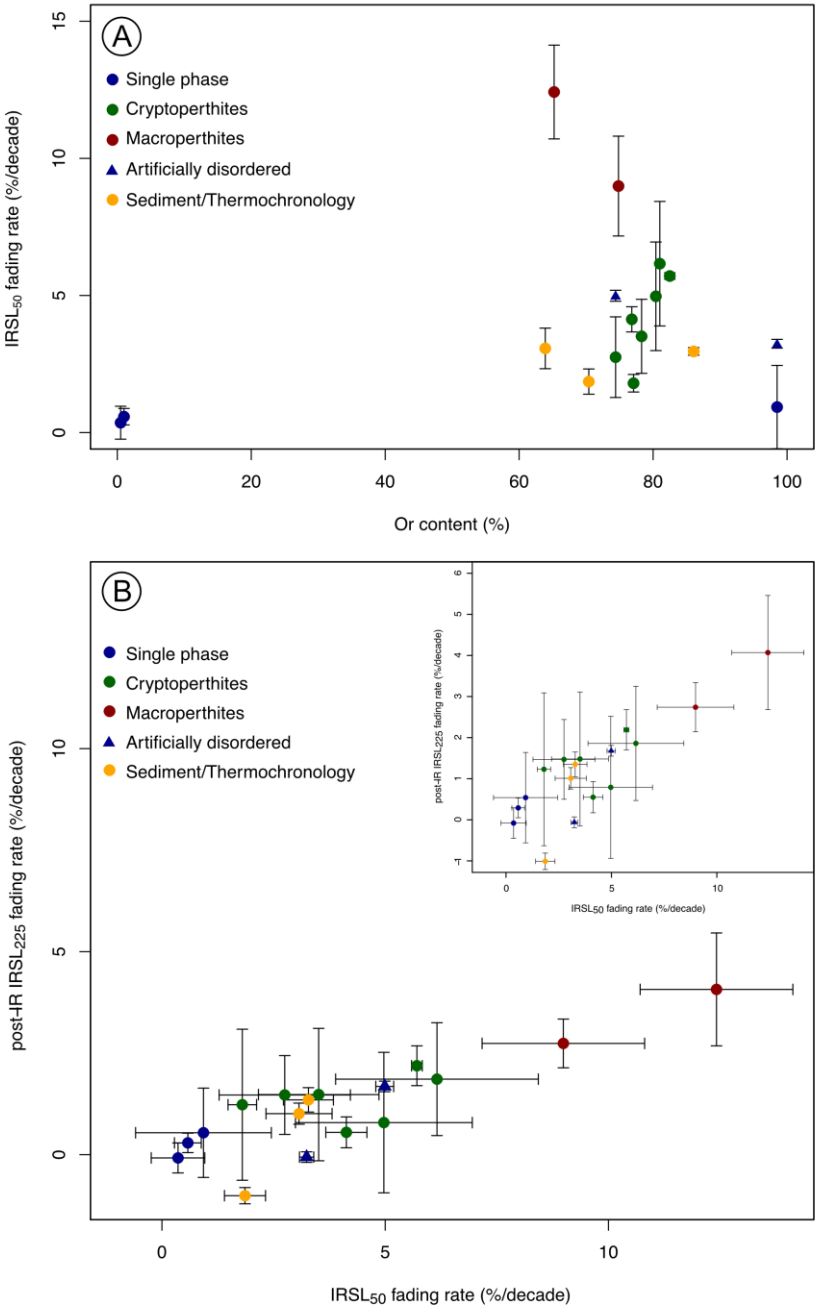

Fig. 8. A) Comparison of fading rates of the post-IR $IRSL_{225}$ signal and the $IRSL_{50}$ signal, obtained using the post-IRIRSL protocol. The inset is a close-up version of B. The data points in A and B are the average fading rate of the measured aliquots for each sample and the standard deviation of these measurements. B) Fading rates for the $IRSL_{50}$ signal measured using a post-$IR_{50}IRSL_{225}$ protocol, with a 250 °C preheat for 60 s.

Exploring sources of variation in thermoluminescence emissions and anomalous fading in alkali feldspars

Supplementary Material

S. Riedesel[1], A.M.T. Bell[2], G.A.T. Duller[1], A.A. Finch[3], M. Jain[4], G.E. King[5], N.J. Pearce[1], H. M. Roberts[1]

[1]Department of Geography and Earth Sciences, Aberystwyth University, United Kingdom

[2]Materials and Engineering Research Institute, Faculty of Science, Technology and Arts, Sheffield Hallam University, United Kingdom

[3]School of Earth and Environmental Sciences, University of St. Andrews, St. Andrews, United Kingdom

[4]Department of Physics, Technical University of Denmark, DTU Risø Campus, Roskilde, Denmark

[5]Institute of Earth Surface Dynamics, University of Lausanne, Lausanne, Switzerland

Figures

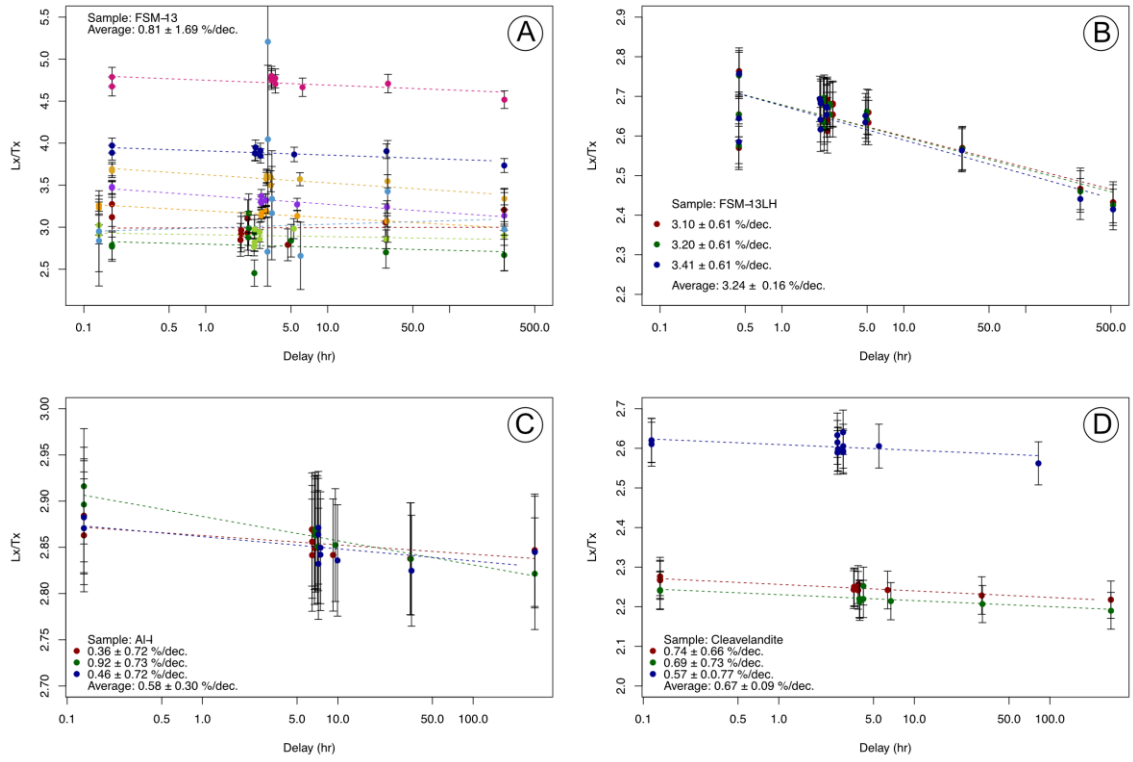

Fig. S1. Fading results as Lx/Tx versus delay time for FSM-13 (A), FSM-13LH (B), Al-I (C) and Cleavelandite (D).

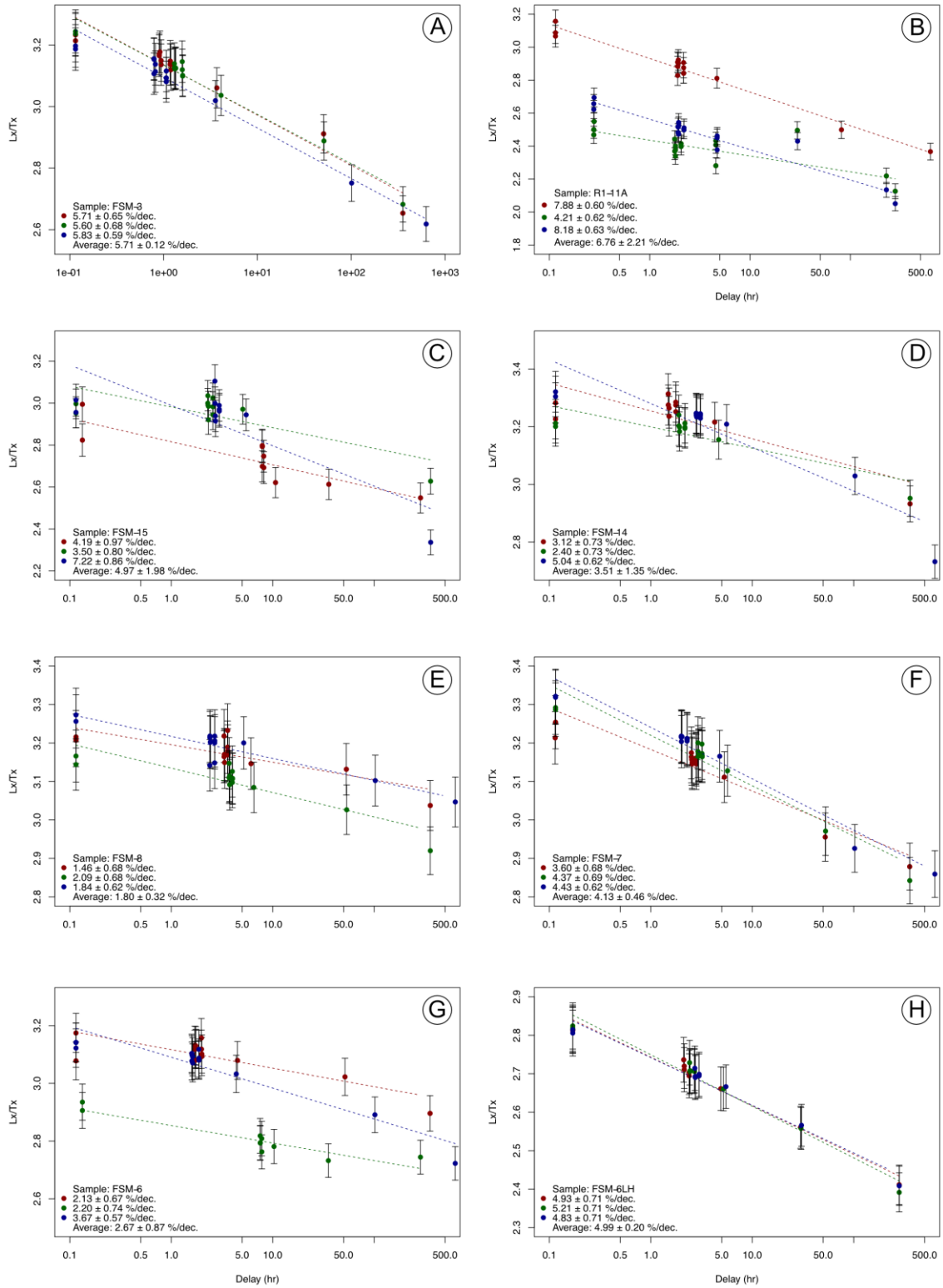

Fig. S2. Fading results as Lx/Tx versus delay time for FSM-3 (A), R1-11A (B), FSM-15 (C) FSM-14 (D), FSM-8 (E), FSM-7 (F), FSM-6 (G) and FSM-6LH (H).

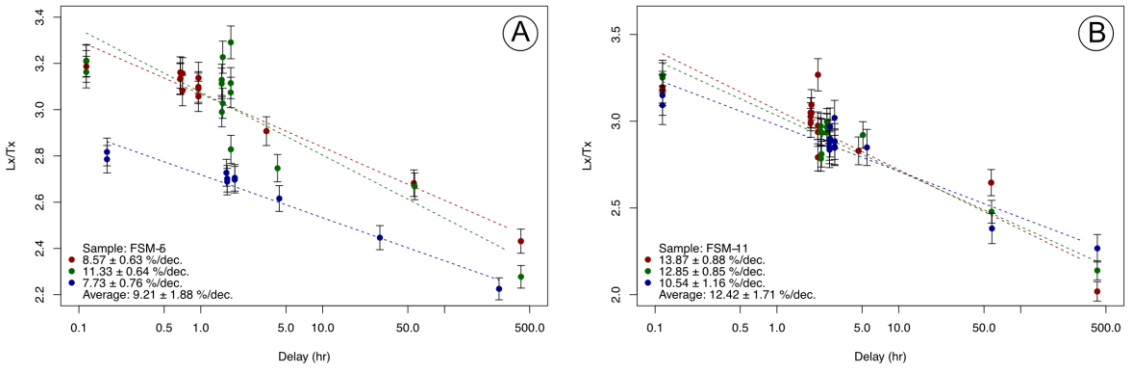

Fig. S3. Fading results as Lx/Tx versus delay time (hours) for FSM-5 (A) and FSM-11 (B).

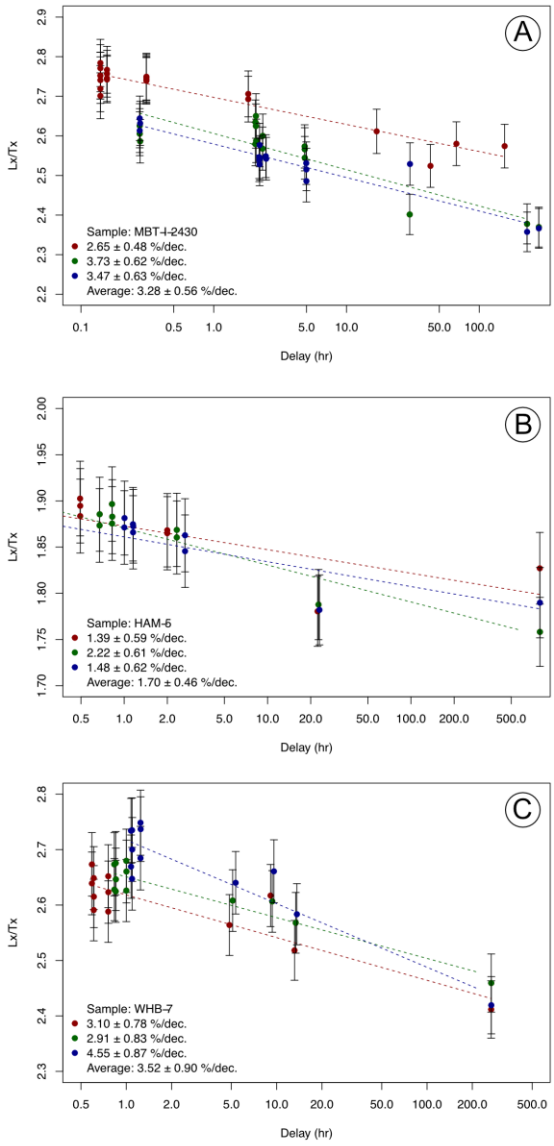

Fig. S4. Fading results as Lx/Tx versus delay time (in hours) for MBT-I-2430 (A), HAM-5 (B) and WHB-7 (C).

Tables

Table S1. Semi-quantitative XRF results (wt%)of samples used in this study, except R1-11A and Cleavelandite.

Oxide	HAM-5	241_WHB-7kf	MBT-I-2430	255_FSM-3	255_FSM-5	255_FSM-6	255_FSM-7	255_FSM-8	255_FSM-11	255_FSM-13	255_FSM-14	255_FSM-15
Al_2O_3	33.80 ± 0.50	20.20 ± 0.60	22.10 ± 0.40	23.50 ± 1.00	21.30 ± 0.50	23.20 ± 1.00	21.20 ± 0.50	25.60 ± 2.00	20.00 ± 0.40	22.00 ± 0.30	21.80 ± 1.00	21.80 ± 1.00
SiO_2	46.00 ± 0.40	65.90 ± 3.00	63.20 ± 2.00	61.40 ± 2.00	62.50 ± 2.00	62.70 ± 0.40	62.80 ± 2.00	55.60 ± 0.60	64.30 ± 2.00	62.00 ± 2.00	61.90 ± 2.00	63.10 ± 2.00
K_2O	14.40 ± 0.10	8.38 ± 0.10	13.00 ± 0.10	13.20 ± 0.10	13.10 ± 0.10	11.10 ± 0.10	12.70 ± 0.10	15.20 ± 0.10	11.20 ± 0.10	15.70 ± 0.10	12.00 ± 0.10	12.60 ± 0.10
Na_2O	3.66 ± 0.20	2.72 ± 0.30	1.33 ± 0.10	1.81 ± 0.10	2.90 ± 0.20.	2.48 ± 0.10	2.39 ± 0.20	2.93 ± 0.20	3.93 ± 0.20	0.16 ± 0.03	2.14 ± 0.10	2.02 ± 0.10
CaO	0.59 ± 0.03	0.72 ± 0.04	0.10 ± 0.01	0.06 ± 0.01	0.00 ± 0.00	0.06 ± 0.01	0.24 ± 0.02	0.08 ± 0.01	0.00 ± 0.00	0.00 ± 0.00	0.09 ± 0.01	0.00 ± 0.00
Fe_2O_3	0.40 ± 0.02	1.23 ± 0.03	0.00 ± 0.00	0.00 ± 0.00	0.00 ± 0.00	0.00 ± 0.00	0.00 ± 0.00	0.00 ± 0.00	0.46 ± 0.02	0.00 ± 0.0	0.00 ± 0.00	0.17 ± 0.01
TiO_2	0.14 ± 0.01	0.02 ± 0.00	0.00 ± 0.00	0.00 ± 0.00	0.00 ± 0.00	0.00 ± 0.00	0.00 ± 0.00	0.00 ± 0.00	0.00 ± 0.00	0.00 ± 0.00	0.00 ± 0.00	0.00 ± 0.00
MgO	0.47 ± 0.04	0.59 ± 0.07	0.00 ± 0.00	0.00 ± 0.00	0.00 ± 0.00	0.00 ± 0.00	0.00 ± 0.00	0.00 ± 0.00	0.00 ± 0.00	0.00 ± 0.0	0.00 ± 0.00	0.00 ± 0.00
Other	0.45 ± 0.02	0.29 ± 0.09	0.21 ± 0.01	0.07 ± 0.00	0.12 ± 0.01	0.40 ± 0.02	0.61 ± 0.02	0.62 ± 0.13	0.19 ± 0.01	0.18 ± 0.00	2.15 ± 0.12	0.26 ± 0.01